UNIVERSIDAD DE CHILE
FACULTAD DE CIENCIAS FÍSICAS Y MATEMÁTICAS
DEPARTAMENTO DE ASTRONOMÍA

DUST TRAPS AND WARPS IN TRANSITIONAL PROTOPLANETARY DISKS

TESIS PARA OPTAR AL GRADO DE MAGÍSTER EN CIENCIAS, MENCIÓN ASTRONOMÍA

SEBASTIÁN MARINO ESTAY

PROFESOR GUÍA:
SIMON CASASSUS MONTERO

MIEMBROS DE LA COMISIÓN:
LUCAS CIEZA GONZALEZ
PATRICIO ROJO RUBKE
LEONARDO BRONFMAN AGUILÓ

Este trabajo ha sido parcialmente financiado por Millenium Nucleus “Protoplanetary Disks in ALMA Early Science” y Beca Magíster Nacional CONICYT

SANTIAGO DE CHILE
2015

Resumen

Actualmente se piensa que los planetas se forman alrededor de estrellas jovenes en discos circumestelares que pueden durar unos pocos Ma. Estos discos *protoplanetarios* evolucionan a traves de diferentes mecanismos. Dos teorías tratan de explicar la formación de un planeta gigante: inestabilidad gravitacional y acreción del núcleo. estos planetas masivos pueden interactuar con el disco abriendo huecos y cavidades en el perfil de densidad superficial.

Estudios detallados de estos huecos en discos protoplanetarios, han revelado estructuras que conducen a investigacion contemporánea. Una de estos rasgos son los dos nulos de intensidad en luz reflejada, vistos en el disco externo de HD 142527. En el Capítulo 1 se propone que estos son sombras proyectadas por un disco interno inclinado. Los discos internos interno y externo son opticamente gruesos en banda H, por lo que la forma y orientación de las sombras informa sobre la estructura tridimensional del sistema. Predicciones de transferencia radiativa de un modelo paramétrico de disco permite concluir que el disco interno está inclinado en $70\pm5^\circ$ con respecto al disco externo.

La teoría de acreción del núcleo plantea que la formación de planetesimales necesita que el polvo crezca de de micrones a kilometros. Trampas de polvo causadas por maximos de presión han sido propuestos como regiones donde polvo puede concentrarse y crecer los suficientemente rápido para formar planetesimales. En el Capítulo 2 se reportan nuevos datos VLA Ka & Ku del disco protoplanetario MWC 758. La imágen Ka muestra emisión compacta en el disco externo indicando una gran concentración de granos grandes. Datos ALMA públicos, trazando granos más pequeños, muestran emisión extendida del disco con un pico de intensidad hacia el noroeste de la estrella, que coincide con el la emisión VLA. Esta segregación de granos de polvo es esperada en la presencia de una trampa de polvo. También se desarrollo un modelo paramétrico no axisimétrico de disco con un vórtice que reproduce las observaciones. Finalmente, comparamos las observaciones radio con datos SPHERE de luz reflejada. El pico VLA está radialmente desplazado de una estructura espiral.

Los discos HD 142527 y MWC 758 muestran desviaciones de simetría axial. Interrogantes teóricas aparecen acerca del origen del disco torcido en HD 142527, pero también este tiene consecuencias dinámicas ya que las zonas de sombra son más frías. Por otro lado, los datos VLA de MWC 758 muestran que los granos grandes están muy concentrados radial y azimutalmente, sugiriendo una trampa de polvo. Es posible que en esta región compacta un planeta pueda formarse por accreción del nucleo. Todas estas asimetrías podrías ser generales para discos, lo que contradice nuestra idea estándar de discos simétricos

Abstract

Planets are thought to form around young stars in circumstellar disk that can last for a few Myr. These *protoplanetary* disks evolve in time through different mechanisms. Two different theories explain how a giant planet might form: gravitational instability and core accretion. These massive planets can interact with the disk opening gaps and cavities in the surface density distribution.

Detailed observations of gaps in protoplanetary disks have revealed structures that drive current research on circumstellar disks. One such feature is the two intensity nulls in scattered light seen along the outer disk of the HD 142527. In Chapter 1 we propose that these are shadows cast by a tilted inner disk. The inner and outer disk are thick, in terms of the unit-opacity surface in H-band, so that the shape and orientation of the shadows inform on the three-dimensional structure of the system. Radiative transfer predictions on a parametric disk model allow us to conclude that the inner disk is inclined by 70 ± 5 deg with respect to the outer disk.

The core accretion theory states that the formation of planetesimals requires that primordial dust grains grow from micron- to km-sized bodies. Dust traps caused by gas pressure maxima have been proposed as regions where grains can concentrate and grow fast enough to form planetesimals, before radially migrating onto the star. In Chapter 2 we report new VLA Ka & Ku data of the protoplanetary disk around MWC 758. The Ka image shows a compact emission region in the outer disk indicating a strong concentration of big dust grains. Tracing smaller grains, archival ALMA data shows extended disk emission with an intensity maximum to the north-west of the central star, which matches the VLA clump position. This segregation of grains sizes is expected in the context of dust trapping, where big grains are trapped more easily than smaller grains in gas pressure maxima. We develop a non-axisymmetric parametric model with a steady state vortex solution which reproduces the observations. Finally, we compare the radio continuum with SPHERE scattered light data. The VLA clump is radially offset of the north-western spiral-like feature.

The disks HD 142527 and MWC 758 present signs of non-axial symmetry. The warped disk in HD 142527 raises theoretical questions about its origin, but also it has consequences in the disk dynamics as the shadowed regions are colder. On the other hand, the VLA data of MWC 758 show that big grains are highly concentrated in radius and azimuth in the outer disk, suggesting dust trapping by a pressure maximum. This compact region is a possible location for planet formation via core accretion. All these asymmetries could be general for disks, challenging our standard picture of axisymmetric disks.

Este trabajo esta dedicado a mi familia y mejores amigos, en especial a mis padres que siempre me impulsaron a perseguir mis sueños.

"Look up at the stars and not down at your feet. Try to make sense of what you see, and wonder about what makes the universe exist. Be curious", Stephen Hawking.

Agradecimientos

Quiero agradecer en primer lugar a Simon Casassus, profesor guía, colaborador, compañero y amigo. Fue mi primer profesor de Astronomía en la Universidad y el primero en motivarme a estudiar la formación planetaria. Simpre tuvo confianza en mis capacidades y siempre me empujó hacia grandes desafíos.

Tambien me gustaría agradecer a Sebastián Perez, gran amigo y ejemplo a seguir, no solo en Astronomía, sino que por su motivación en distintas disciplinas.

Además, me gustaría agradecer a Rafael Cautivo, profesor de física durante mis estudios de enseñanza media. Él fue una fuente de inspiración para estudiar ciencias físicas y buscar mis propias respuestas.

Por último, quiero agradecer a mi familia, en especial a mis padres que nunca dudaron del camino que elegí seguir y me empujaron a perseguir mis sueños.

Contents

List of Tables

List of Figures

Introduction

The origin of the Solar System has been one of the main fundamental questions in Astronomy, both in in the past and in modern research. It was even considered part of cosmology studies. One way to study its origin is to look at young stars that are currently forming planets, and look at the physical process going on in those systems through multiwavelength observations and numerical simulation.

Since after the discovery of 51 Pegasi b in 1995, which is the first exoplanet discovered around a main-sequence star [96], we know there are other planets around stars, and the question of "how abundant exoplanets are?" was close to being answered. Twenty years later, we have found more than a thousand of new exoplanets, most of them discovered by large exoplanet surveys using different techniques: transits [9], radial velocities [97, 144], microlensing [28], and even some of them were directly imaged [72, 76, 79, 95, 119]. These findings have demonstrated that planets around main sequence stars are frequent. The current statistics indicate that almost every star hosts at least one planet [18, 28, 97], thus, try to understand the planet formation mechanisms has become also missing piece of the puzzle of planetary science.

0.1 Early thoughts and theories about planet formation

The first ideas about planet formation can be traced back to 1644 when Descartes wrote a discussion about the Earth formation and the rest of the planets and satellites [39]. In his book he states that the solar system formed from at least fourteen vortices. The biggest vortices gave rise to the Sun, Jupiter and Saturn. He also mentions that the "stars" surrounding Jupiter were also formed from small vortices that then descended towards Jupiter.

A century later in 1755, the Philosopher Immanuel Kant developed a theory called "The Nebular Hypothesis" [73] in which he proposed that the solar system formed from a gaseous flat cloud, slowly rotating and collapsing. It is very surprising how early in history the idea of planets forming from a disk surrounding the Sun appeared, matching the basic principles of our current theories.

Then in 1944, C.F. Wizsäcker discussed about the origin of the Solar System [52]. In his work he argue against the theory that planets formed from a solar ejection of material, which was a popular theory in that time, saying that such an event could not explain why most

of the angular momentum of the Solar System is on the planets. He proposed that planets formed from a thin rotating cloud around a primitive Sun, of a tenth of the Solar mass. In this disk, planets would form from the interaction between vortices and thus, giving the right orientation to the rotation of planets. An important consequence of Wizsäcker's theory is that planetary systems of a wide variety of types has to be common in the Universe.

A more quantitative description of the planet formation theory and very close to our current picture was developed in the 60s by Viktor Safronov [123]. He described the evolution of the Protoplanetary Cloud and formation of the planets by core accretion: large bodies or "planetary embryos" accumulating material through collisions enhanced by the gravity of the largest bodies. Safronov was also the first to introduce the idea of what was going to be known as "minimum mass Solar Nebula" [139]. Based on the mass, orbital radius and composition of the planets in the Solar System, and assuming that the mass of the original circumstellar disk in solid bodies was conserved at all times and at each radius, it is possible to estimate roughly a lower limit for the disk mass that formed the bodies in the Solar System.

0.2 Current theory of planet formation

Current theories of star and planet formation state that disk forms around a pre-main sequence star after the gravitational collapse of a molecular core. These diffuse clouds cannot collapse immediately onto the core because they have too much angular momentum. Instead they form a disk as a consequence of conservation of angular momentum. They are composed of gas and dust with chemical abundances similar to the primordial molecular cloud, and observations show that these disks are present in young stars for the first few million years of their evolution [93, 127]. These circumstellar disks are called *protoplanetary disks* because they will give birth to planetary systems around the stars.

0.2.1 Observational studies

Observational studies of protoplanetary disks involve a wide variety of observations at different wavelengths. They cover from the near-infrared (NIR), where most of the emission comes from stellar light scattered by dust grains in the disk and the thermal emission coming from the very hot dust near the star; to radio wavelengths, where pure thermal emission coming from cold disk regions can be detected, although some free free emission coming from the innermost parts has been detected at radio frequencies. After the *Infrared Astronomical Satellite* (IRAS) was launched, the first statistical studies of protoplanetary disk started by measuring NIR excess in young stars [127]. Thanks to the development of very sensitive receptors at millimeter wavelengths shortly after, it was discovered that these disks have dust with grain size distribution that can reach centimeter sizes, proving that grain growth can occur in these disks, e.g. [140].

Using multiwavelength observations it is possible to reconstruct the spectral energy distribution (SED) of disks. Although some degeneracies exist, disk modelling to fit SEDs has

been fundamental to infer their physical structure. In addition, thanks to molecular line observations, kinematic studies are possible. Disk inclinations (i), position angles (P.A.) and rotational profiles can be derived from Doppler shift studies, showing that in general protoplanetary disks are in Keplerian rotation. However, some disks present strong deviations from Keplerian rotation that could be linked to warped structures and high radial velocity components.

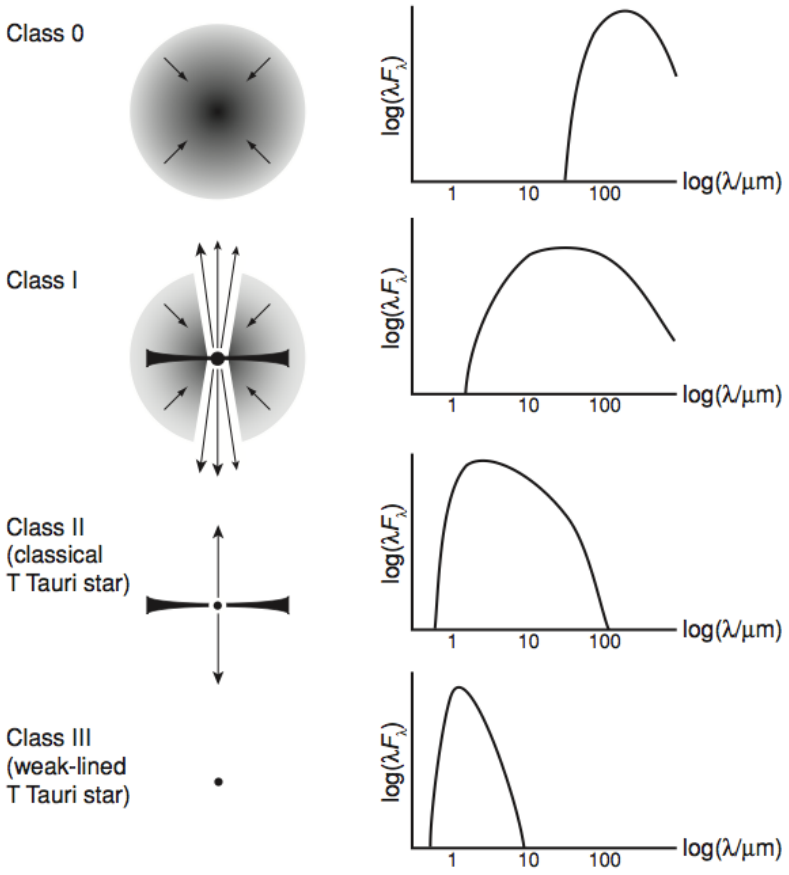

Figure 1: Classification scheme for Young Stellar Objects from [5].

Space telescopes together with ground-based 8-meter class telescopes, with adaptive optic systems, have allowed to directly image protoplanetary disks in the optical and NIR. Using different techniques it is possible to subtract the stellar point spread function (PSF), e.g. angular differential imaging (ADI), polarized differential imaging (PDI) or using a coronagraph. The former allows searching for forming planets in protoplanetary disks as it can be very sensitive to detect point-like sources embedded in disks. On the other hand with PDI it is possible to make images of the polarized intensity which traces the surface of a disk. This is because the stellar light or hot thermal emission scattered by dust grains becomes polarized after an scattering event. All these images reveal that protoplanetary disks spans from tenths to hundreds astronomical units (aus), with aspect ratios of $\sim$0.1.

From observations Young Stellar Objects (YSOs) have been divided into classes depending on their SED. Three classes were suggested originally [77], and then expanded with a class 0 [3], to complete four categories of YSOs: 0, I, II & III, each related to a particular evolutionary

stage of a pre-main sequence star and circumstellar disk. The class of a particular object is usually determined by measuring the slope of the SED between 2 and 25 μm (see figure 1).

Class 0 represents a protostar completely embedded in infalling circumstellar material that reprocesses the stellar radiation to longer wavelengths. Class I objects represent a second stage when the central star accretes matter through a disk, but it is still embedded. Strong stellar winds and bipolar outflows are common at this stage, and it lasts ~ 0.5 Myr [47]. Class II objects represent the stage when most of the surrounding material has been dissipated by stellar winds. This stops the infall of material and what remains is the star and an optically thick disk in the NIR. Their SED is the sum of the stellar spectrum and the circumstellar disk thermal emission from the IR to radio wavelengths. UV-excess is also common as there is still accretion onto the star. This is the phase when massive planets are suppose to form, when there is still a high mass reservoir in the disk ($\sim$10% of the stellar mass) and because planet formation via core accretion takes a few Myr (see Section 0.2.4) . Finally Class III objects represent zero age main-sequence stars with very low NIR excess. In the class III stage all that remains is the result of the planet formation process: planets, asteroids, comets, and small dust grains that are quickly blown away by radiation pressure or they fall onto the star due to Pointing-Robertson effect. However, dust can be replenished as a result of the collision between large bodies [145]. At this stage all the circumstellar gas has been dissipated (see Section 0.2.3). These *debris* systems are called debris disks.

Multiwavelength observations

Protoplanetary disks studies require multiwavelength observations because different wavelengths trace different regions of disks. Dust temperature decreases with radius, thus, thermal emission at short wavelengths, e.g. NIR, will highlight the hot inner regions and surface of the disk ($r \lesssim 5$ au), while at longer wavelengths, e.g. (sub)millimeter, the outer and cold regions of the disk stand out ($r \gtrsim 5$ au). Figure 2 illustrates the different regions of a typical protoplanetary disk and what techniques are used to study the different regions. While VLTI can image the inner regions of disks in the NIR and MIR, ALMA and other radio interferometers also study the outer parts of disks.

0.2.2 Disk structure

The structure of protoplanetary disks depend on several factors. They are typically treated as axisymmetric, with their physical properties depending only in radius r and the vertical coordinate z. The radial structure of disks is expected to evolve with time due to viscous evolution, accretion, photoevaporation and magnetohydrodynamic (MHD) effects where ionization is important. Moreover, the stellar irradiation of field stars or the gravitational perturbation of a flyby can be also important in the disk structure and evolution, specially in high stellar density environments. Disks are typically parametrized with a power law:

$$\Sigma(r) = \Sigma_c \left(\frac{r}{r_c}\right)^{-\gamma}, \tag{1}$$

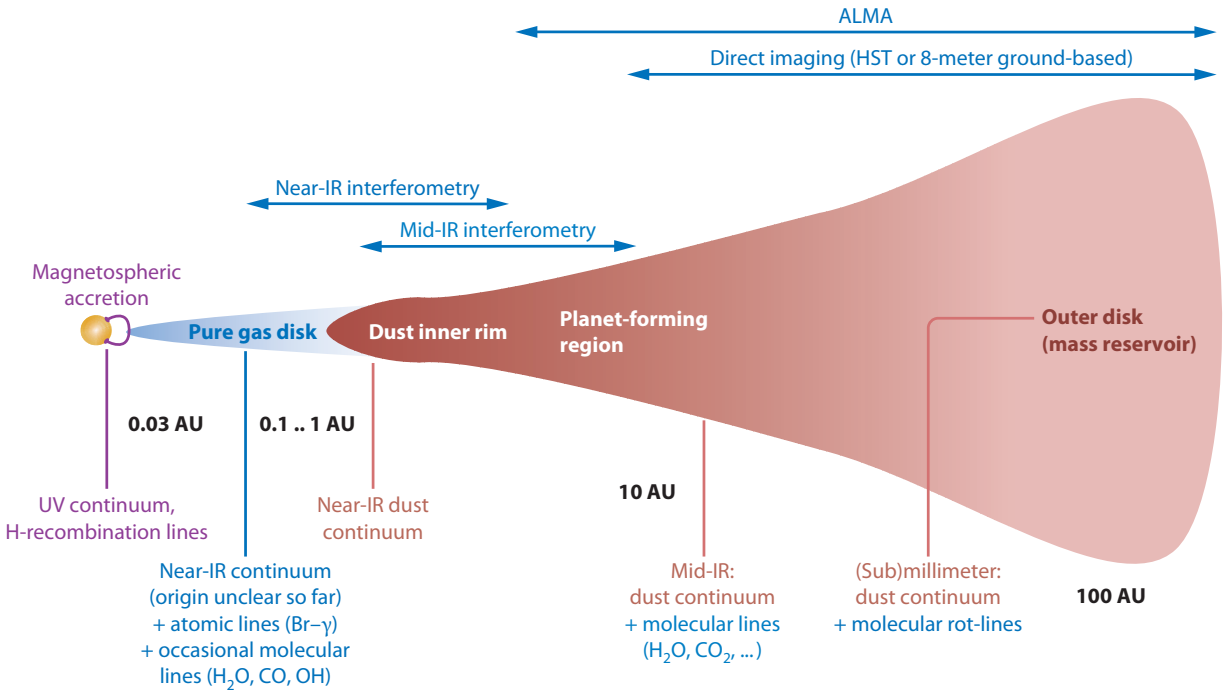

Figure 2: Illustration of the structure and spatial scales of typical protoplanetary disk. Above the disk different observational techniques are listed, showing the region of disk that they can study. In the bottom the type of emission that emerges at different radii. The illustration was taken from Dullemond & Monnier 2010 [42].

where γ controls how steep is the surface density distribution. The radial density distribution obeys to an equilibrium between the stellar gravity force, the centrifugal force, viscous evolution and the radial pressure gradient.

Vertically, disks are assumed to be in hydrostatic equilibrium. Neglecting the self-gravity of the disk, the vertical component of the stellar gravity g_z has to be balanced by the gas pressure gradient. If we assume disks are vertically isothermal, the pressure can be written as $\mathrm{P} = \rho\, c_s^2$, with c_s the sound speed. This yields

$$c_s^2 \frac{\mathrm{d}\rho}{\mathrm{d}z} = -\frac{GM_* z}{(r^2+z^2)^{3/2}}\rho. \tag{2}$$

The solution to this differential equation is

$$\rho = C \exp\left[\frac{GM_*}{c_s^2 (r^2+z^2)^{1/2}}\right]. \tag{3}$$

Disks are expected to be thin with small aspect ratios, i.e. $H/r \ll 1$, as they have large areas through which they can cool via radiative processes. Taking this into account and defining the scale height $H \equiv \frac{c_s}{\Omega_K}$ (Ω_K is the Keplerian orbital angular velocity), it is easy to

find a simple expression for the vertical mass distribution at a radius r:

$$\rho(r,z) = \Sigma(r)\frac{\mathrm{e}^{-\frac{z^2}{2H^2}}}{\sqrt{2\pi}H} \tag{4}$$

H depends on Ω_K and c_s, which are both functions of r. Given a typical power law radial profile for the disk temperature, the scale height is $H(r) \propto r^{\alpha}$ with α close to 1. The value of α has consequences in the disk temperature. A disk with $\alpha > 1$ will have higher temperatures at large radii than a disk with $\alpha < 1$ because of the higher direct stellar irradiation at large radii.

Until now, we have assumed that disks lie in a single plane as they are axisymmetric structure. However, the presence of a companion (e.g. forming planet, binary, or even a fly by) or a more complicated disk envelope interaction could break the axisymmetry producing spiral waves, warping the disk, inducing highly inclined orbits and eccentricities of the solid bodies in the disk. Chapter 2 presents evidence of a warped structure in the HD 142527 protoplanetary disk.

Aerodynamic drag

In the book by Armitage *Astrophysics of Planet Formation* [5], aerodynamic drag is discussed in details, here we present a summary of the main ideas As it was mentioned before, disks are composed of gas and dust. Dust grains act as test particles that are under the influence of stellar gravity, but also under the aerodynamic drag forces by the gas. They can have different vertical, radial and azimuthal density distributions compared to the gas. Typically, dust grains would accumulate around gas pressure maxima due to drag forces [20, 111].

Defining the friction time scale for a particle of mas m as

$$t_{fric} = \frac{mv}{F_D}, \tag{5}$$

where v is the relative velocity between the dust particle and the gas, and F_D is the drag force produced by the gas on the dust grain. The friction time scale is the time scale at which drag forces will change the grain velocity v. In the Epstein drag regime, i.e. when the size of dust grains is smaller than the mean free path of gas particles, and considering grain velocities much lower than the mean thermal speed, the drag force can be written as

$$F_D = -\frac{4\pi}{3}\rho a_s^2 v_{th} v, \tag{6}$$

where ρ is the gas density, a_s is the radius of a spherical dust particle and v_{th} is the mean thermal speed. Using that the particle mass $m = (4/3)\pi a_s^3 \rho_s$, with ρ_s the internal density of dust grains, the frictional time scale can be re-written as

$$t_{fric} = \frac{\rho_s}{\rho}\frac{a_s}{v_{th}}. \tag{7}$$

It is common to define the *Stokes number* St as the ratio of the friction time scale and the orbital period, i.e. $\mathrm{St} = t_{fric} \times \Omega_K$. Using that $v_{th} = \sqrt{8/\pi} c_s$ and $H = c_s/\Omega_K$, St take the form of

$$\mathrm{St} = \sqrt{\frac{\pi}{8}} \frac{a_s}{H} \frac{\rho_s}{rho}. \tag{8}$$

When dust particles have a $\mathrm{St} \ll 1$ they are completely coupled to the gas and they have a spatial distribution equal to the gas. However when $\mathrm{St} \sim 1$ particles partially decouple from the gas, so that dust trapping in pressure maxima becomes important, as the dust settling in the midplane of the disk [20, 111].

Another important consequence of aerodynamic drag is that big dust grains are completely decouple from the gas ($\mathrm{St} \gg 1$), hence they orbit at Keplerian velocities. However, the gas in the disk rotates typically at sub-Keplerian velocities due to the negative radial gradient of the gas pressure. This difference in orbital velocities at the same radius causes a constant drag in big dust grains and hence, they drift radially towards the central star [138]. This can be avoided if the radial pressure gradient becomes positive at a given radius.

0.2.3 Disk lifetime and dispersal mechanisms

Thanks to well established correlations between the presence of NIR excess, spectroscopic signatures of accretion and stellar age [59], it is possible to study the lifetime of the inner regions of disks. NIR studies with IRAS and ISO ($1-5$ μm) have shown that 60-80 % percent of young stars with ages ≤ 1 Myr present measurable NIR excess (i.e. disks), while just a 10% of disks older than 10 Myr present an excess [127]. At longer wavelengths ($3.6-8.0$ μm and 24 μm) *Spitzer* obtained similar results [56, 63, 78, 125, 128, 143]. However large uncertainties still remain in stellar ages at early times.

At sub-millimeter wavelengths disks are normally optically thin and the emergent intensities trace the outer parts of protoplanetary disks, where the bulk of the mass lies, thus it is possible to derive disk masses in dust. Figure 3 shows disk masses derived from sub-millimeter studies for several stars with different spectral types and ages. In general disk masses decrease with age and an abrupt drop in the disk mass appears at ~ 10 Myr, very similar to what NIR and MIR studies show. This coincidence suggests that once the inner regions of the disk disappear and accretion stops, the rest of the disk disappears as well. After that disks are called debris disks, although there is an age overlap.

In addition, observations of young stellar clusters and associations show that disk lifetimes have some dependence on the spectral type or stellar mass. Disks around massive stars disappear faster than solar-mass stars [142].

These results show dust at different radii can last ~ 10 Myr, but after that, dissipation occurs in a much shorter time scale of $\lesssim 0.5$ Myr [34]. Thus, what is the physical process that controls disk lifetime? During their life disks evolve through different mechanisms such as viscous evolution, photoevaporation and planet disk interactions. Understanding these processes is crucial because the disk lifetime sets a time limit for planet formation.

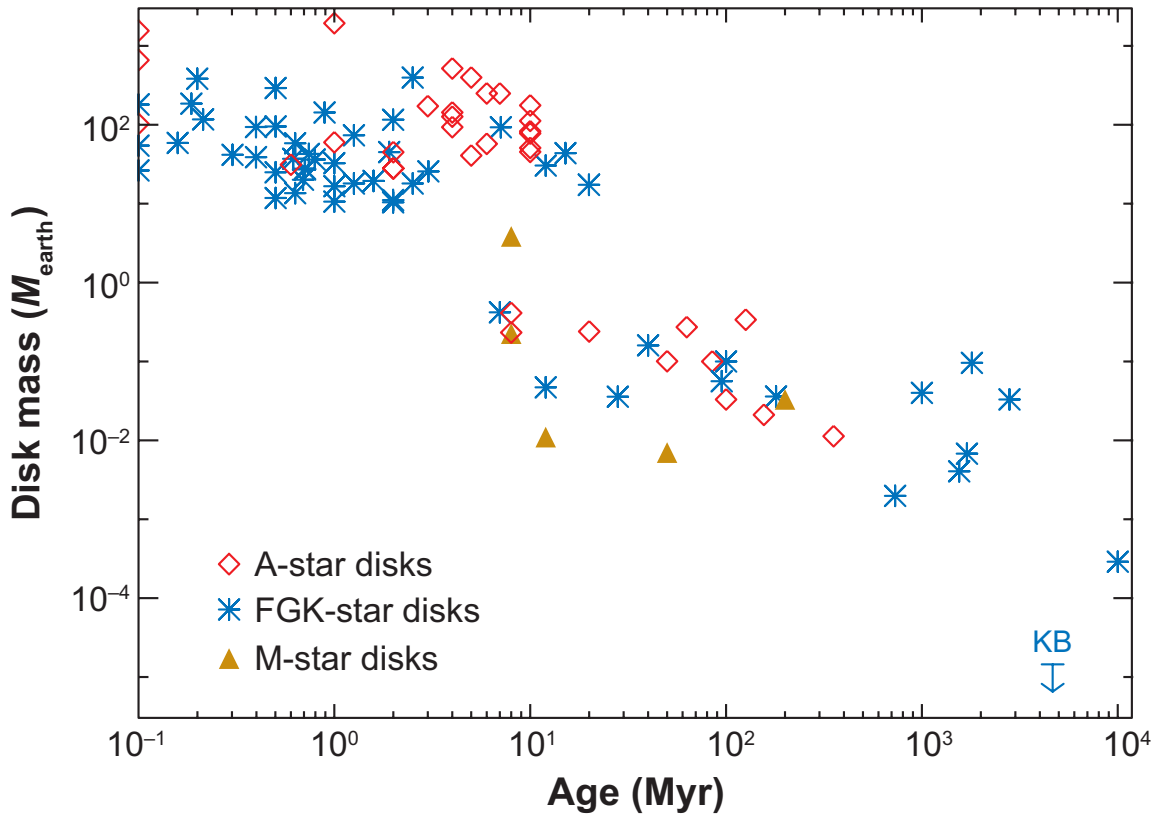

Figure 3: Disk mass evolution derived from sub-millimeter observations. Figure from Wyatt 2008 [145].

For a Keplerian disk, accretion requires gas must loose its angular momentum through some mechanism. Solutions to hydrodynamic equations for viscous fluids show protoplanetary disks must evolve: gas accretes onto the star and spreads difussively to large radii carrying the angular momentum outwards [6]. In addition, viscosity acts as a means through which the disk can dissipate energy. MHD simulations have been successful in reproducing the decrease in accretion over time [60] and emission line profiles [104]. However pure viscous models fail in reproducing the short time scale disk dissipation and the variety of SEDs observed.

Moreover, the central or field stars are also important for the disk evolution. Disk models that combine viscous evolution with photoevaporation are able to reproduce the disk evolution time scales [1, 2, 35].

Planet disk interaction might be also important for the protoplanetary disk structure and evolution. Massive planets can open gaps in the surface density distributions [84, 86], trapping bigger dust grains at the outer parts of the disk [20, 111]. Moreover, vortices can be induced by planets triggering the formation of second generation planets by core accretion [8, 67, 71, 89, 91, 92, 120, 129].

0.2.4 Two main theories to form a planet

Two main theories try to explain the formation of a gas giant planet: "Gravitational Instability" and "Core Accretion". They differ in the physical mechanism and time scales of planet formation, but they are not exclusive. Both process can occur in the same disk, but probably at different stages of the disk evolution.

Gravitational Instability

When disks are young and massive, self-gravity can be important in the disk dynamics. Neglecting the MHD effects on the disk, the stability of the disk is set by a balance between gravity, radiative cooling, pressure and shear. While the disk gravity and radiative cooling push the disk to fragment into clumps, pressure helps to support the disk at small scales. On the other hand shear stabilises the disk at large scales destroying large structures due to differential rotation [6].

For a thin Keplerian disk, a simple estimate of the linear stability of an overdensity can be computed with the Toomre Q parameter [132], originally proposed to study the stability of a disk of stars. Q can be defined as:

$$Q \equiv \frac{c_s \kappa}{\pi G \Sigma}, \tag{9}$$

where c_s is the sound speed, κ is the epicyclic frequency, defined as the frequency at which a particle oscillates with respect to a radius when it is slightly displaced radially, and Σ is the disk surface density at a given radius. If the disk is massive, perturbations will grow exponentially rather than propagate as a pressure wave. Radial perturbations will grow exponentially if $Q < 1$, although a more general 2D treatment shows perturbations can grow if Q is lower than 1.5 [106].

Low mass disks ($M_{\mathrm{dis}k} \ll M_*$) can be assumed to be in almost Keplerian rotation, i.e. $\Omega_K(r) \propto r^{-3/2}$. Thus the epicyclic frequency can be written as $\kappa^2 \equiv (2\Omega_K/r)\frac{\mathrm{d}}{\mathrm{d}r}(r^2\Omega_K) \approx \Omega_K^2$. Using the last approximation and the previous definition of the scale height in terms of c_s and Ω_K, Q can be re-written as

$$Q \equiv \frac{H M_*}{\pi \Sigma(r) r^3}. \tag{10}$$

This means that if $\Sigma(r) > H M_*/\pi r^3$ the disk will become locally unstable. Thus, gravitational instabilities are more likely to occur at the earliest phases when the disk is more massive and at larger radii for disks with flat surface density profiles, i.e. $\Sigma(r) \propto r^{-\gamma}$ with $\gamma \leq 3$.

This condition ignores the cooling time scales t_{cool} of the gas which, if it is too large, can prevent the local grow of perturbations. The outcomes of the instabilities are not easy to treat analytically and numerical methods are used to study the different possibilities. The disk can develop self-gravitating turbulence with spiral arms transporting angular momentum outwards via gravitational torques [87]. A second possibility is that the disk instabilities

could produce bursts of accretion. A third possibility is that the disk can fragment. In the last scenario massive planets or substellar companions can form [17, 19, 126].

In summary, massive planets will form via gravitational instabilities at large radii and at earlier phases where and when the Q parameter is lower. One of the goals of current research projects is to estimate Q in protoplanetary disks that present spiral arms that could be triggered by gravitational instabilities. However, disk mass estimates have been elusive due to the lack of a good tracer for the gas mass in disks.

Core Accretion

The second mechanism proposed to form a giant planet or even a terrestial planets is via core accretion. This theory states that planet formation requires the build up of a population of planetesimals. To form these bodies, dust grains need to grow from micron to kilometer sizes, i.e. grains need to increase in size by at least nine orders of magnitude in size scale via two body collisions, until the influence of gravity enhances protoplanet growth [113, 124].

Once the core reaches a critical mass, it triggers an hydrodynamic instability in the disk causing fast gas accretion onto the core [100, 109]. For standard disk parameters the critical mass is $\sim$10 $M_{\oplus}$. This process is a race against the disk dispersal process [35, 65] and accretion onto the central star [60].

One of the big puzzles of this theory is that when particles grow, they tend to move faster in the disk as they decouple from the gas. When they reach a size close to a meter, if not less, they reach a peak velocity that can be as big as 100 m/s. This causes two big problems that are commonly called as the "meter-size barrier". First, when they decouple from the gas they start to drift radially towards the central star [138], therefore planetesimal formation has to happen in time scales shorter than radial drift. The other big problem is that with such high velocities, collisions between big particles result in the fragmentation of big bodies into small particles preventing the collisional growth [57]. However laboratory experiments have shown that impacts of small particles at high velocities are not always erosive [75, 130]

One way to halt the inward drift is by developing a local maximum in the radial surface density of the gas. Dust grains can easily get trapped in density maxima [8, 58, 141], especially big grains [20, 111]. Dust traps can be found in the inner edges of disks with evidence of gaps and cavities, commonly called transitional disks [46]. These gaps and cavities are also detected as infrared dips in the SED. In these dust traps, and depending on the level of gas turbulence, grains can accumulate for periods comparable to the disk lifetime. Thereby benefiting grain growth, and producing an enhancement in the population of larger dust grains [20, 111].

Azimuthal asymmetries, such as vortices, can also produce dust trapping [8, 67, 71, 89, 91, 92, 120, 129]. Large scale asymmetries are observed in sub-millimeter observations of the transition disks around SAO 206426, SR 21 [107], LkHα 330 [70], and particularly in HD 142527 [25, 51] and IRS 48 [135], where a stronger than usual azimuthal contrast is observed. These observations suggest dust trapping by large-scale vortices, although no

kinematic evidence exist to support the vortex scenario in these systems. In this scenario it is expected that the dust spatial distribution will depend strongly on the grain size, as aerodynamic drag depends on the grain cross section. Big grains will concentrate in more compact regions than small grains [41, 67, 74, 89, 99, 116]. This has strong observable implications: at long wavelengths, dust continuum emission should be more compact than at shorter wavelengths, as it traces the mass distribution of grains with sizes comparable to the observed wavelength [10, 15, 131]. Thus, in the absence of tracers of the gas mass, it is crucial to use multiwavelength observations to diagnose dust trapping around a pressure maximum.

A summary of these theories of planet formation, protoplanetary disk evolution and debris disk are well summarized in the reviews of Dullemond & Monnier 2010 [42], Armitage 2011 [6], William & Cieza 2011 [142] and Wyatt 2008 [145].

0.3 This work

This work is about the study of asymmetries in well known protoplanetary disks that could bring clues about the planet formation process and planet disk interaction. It is divided into two main chapters. Each represents a independent research paper.

Chapter 1 titled "Shadows cast by a warp in the HD 142527 protoplanetary disk" was published in *The Astrophysical Journal* the 7th of January 2015. The authors of this paper are Sebastian Marino as first author, with the collaboration of Dr. Sebastian Perez and Professor Simon Casassus. In this first chapter we study two decrements seen in published PDI images of the outer parts of the transition disk around the star HD 142527. We introduced a new interpretation for these decrements presenting a parametric three dimensional disk model of a warped or tilted inner disk. It is inclined by 70 degrees with respect to the outer disk, casting shadows of the stellar light in the outer disk at the position of the decrements. This bears important dynamical consequences in the disk dynamics and rise questions about the origin of such a warp. This chapter also adds some additional material related to ALMA observations that support the warp scenario.

The second chapter is titled "Compact dust concentration in the MWC 758 protoplanetary disk". The work presented in this chapter has been submitted to the *The Astrophysical Journal* on May 22nd of 2015. The first author of that paper is Sebastian Marino, and this work was in collaboration with Professor Simon Casassus, Dr. Sebastian Perez, Dr. Wladimir Lyra, Dr. Pablo Roman, Dr. Christopher Wright and Dr. Sarah Madison. Chapter 2 presents new VLA observations at 15 and 33 GHz of the transition disk around the star MWC 758. The VLA images show very compact emission coming from the disk at the same position where archival ALMA data shows a peak intensity. The VLA clump and ALMA non-axisymmetric disk image can be interpreted as a case of dust trapping by a pressure maximum. We also compare the VLA data with a new reduction of archival SPHERE data.

Finally in Section 2.5 we present the conclusions of Chapter 1 and 2, summarising the new findings, new questions and the implications on these systems and to the rest of proto-

planetary disks.

Chapter 1

Shadows cast by a warp in the HD 142527 protoplanetary disk

1.1 Introduction

The study of planet formation is rapidly being revolutionized by observational breakthroughs, such as the direct images of protoplanetary gaps in near-infrared scattered light. A particularly interesting target is the Herbig Ae/Be star HD 142527, at a distance of ∼140 pc. The disk surrounding HD 142527 boasts the largest inner cavity known, with a ∼1 arcsec radius and seen at a close to face-on orientation, with an inclination of about 24 deg [49, 50]. Improvements in K_s-band coronagraphy revealed fine structure in the outer disk, including two intriguing intensity nulls [22] that break the continuity of the outer disk. In this Letter we propose that these are shadows cast by a warped inner disk.

Recent polarized differential imaging (PDI) of HD 142527 at H- and K_s-bands revealed a striking view of its dust-depleted gap, outer disk and spiral structures [7, 21, 121]. These H-band polarized intensity images outline the outer-disk nulls with the best available detail thus far. One null is found ∼11.5h (North of the star), and the other is found at 7h (South). The Northern null is particularly puzzling as it coincides with the location of the dust density peak, whose spatial distribution is shaped into a large crescent [25, 51, 105]. Thus the Northern null cannot be interpreted as a lack of material.

As witnessed by a bright thermal IR central point source, well in excess of the photospheric emission, the large dust-depleted cavity of the HD 142527 disk is in fact a gap [49, 118, 137]. While knowledge of the outer edge of the gap is limited by theory rather than observational detail, the inner regions of the gap are poorly resolved. A $\sim 10^{-7}\ M_\odot\ \mathrm{yr}^{-1}$ stellar accretion rate [53] would quickly deplete the inner disk, whose dust mass is estimated at $\sim 10^{-9}\ M_\odot$ [137]. This inner disk can be thought of as a transient feature of stellar accretion: it is the convergence point of matter being accreted from the mass reservoir in the outer disk [23, 25, 27]. Long-baseline optical interferometry (VLTI) has resolved this inner disk, and found it to be highly crystalline [133] —but its orientation and extent remain elusive.

Motivated by our research on the intra-cavity gas kinematics [23, 27] we considered the possibility of a continuous warp linking different orientations between the outer and inner disks. The underlying parametric disk model is documented in Section 2.3.4, along with the radiative transfer setup we implemented to calculate the emergent specific intensity fields. Our results are presented in Section 1.3. While the inner disk intercepts stellar light, shadows are cast on the outer disk such that their shape and orientation are sensitive measures of the inner disk orientation. We briefly consider the consequences of this finding in Section 1.4. Finally in Section 1.5 we present the main conclusions of this chapter.

1.2 Parametric modeling

1.2.1 Underlying physical structure

We constructed a synthetic model of HD 142527 inspired by multiwavelength observations and gas kinematics, and detailed enough to provide a comparison point with the near-IR scattered light images as well as the radio continuum emission and gas kinematics. This synthetic model matches the observed spectral energy distribution (SED). Here we document the aspects of the model that are relevant to this work on the H-band images.

The model consists of a star at the center of a dusty disk separated in 3 zones with different density structures, dust grain size distributions and compositions: an inner disk, a gap and an outer disk. A schematic render of the model is provided in Figure 1.1. We model the star using a Kurucz template spectrum [29] at a temperature of 6250 K and with a radius of 3.0 $R_{\odot}$, to fit the SED, being consistent with an extinction of A_V =0.6 [137].

The inner disk starts at 0.3 au and cuts off at 10.0 au. It is described by a surface density proportional to r^{-1} and a scale height of 1.0 au at 10 au with a flaring exponent of 1.1. It is composed of amorphous carbon and silicate grains with sizes between 0.1 to 2.5 μm, with a total dust mass of 5.0×10^{-9} $M_{\odot}$. We introduce an inclination of α=70° to this region with respect to the outer disk midplane.

The gap spans 120 au from 10.0 au. It is described by a surface density proportional to r^{-1} and a scale height of 18 au at 100 au with a flaring exponent of 1.6. It is composed of amorphous carbon and silicate grains with sizes between 1.0 to 10.0 μm. The total dust mass of this section is 1.0×10^{-8} $M_{\odot}$. The disk in this section connects the inner and outer regions varying the inclination linearly from 70° to 0° between 10 and 15 au, where it matches the outer disk orientation. A larger warp would have been obvious in the ^{12}CO kinematics inside the gap [108], with a concomitantly larger region where the inclination crosses the plane of the sky.

Finally, the outer disk extends over 115 au to 300 au with a rounded disk wall between 115 to 140 au. It is composed of 3.0×10^{-6} $M_{\odot}$ of amorphous carbon grains with sizes ranging from 1 to 10 μm and 1.0 $\times10^{-2}$ $M_{\odot}$ of silicate grains with sizes ranging from 100 μm to 5 cm. The dust masses inferred in our models are biased by the lack of grain porosity. The resulting dust masses are also directly affected by uncertainties on the internal densities.

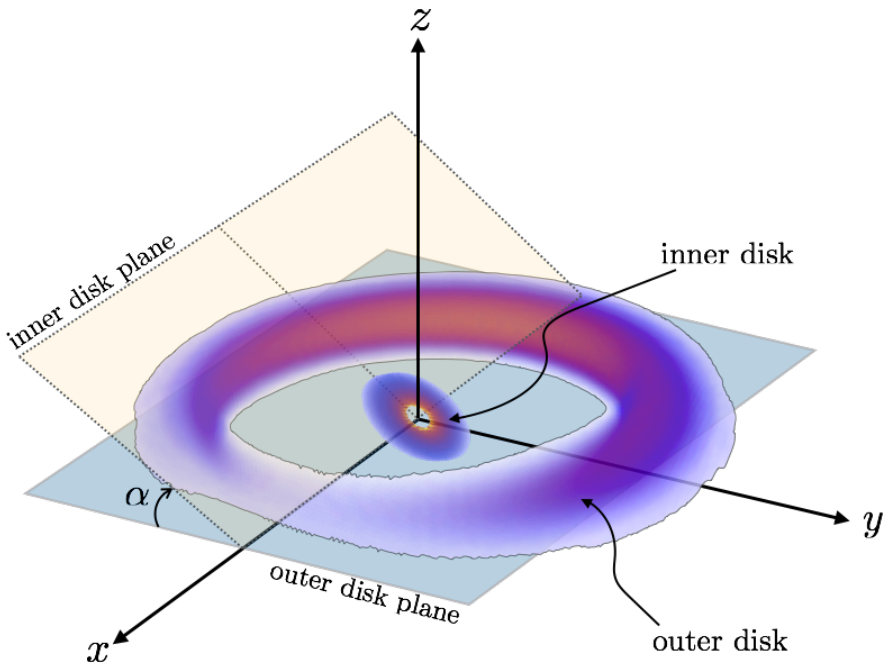

Figure 1.1: Schematic view with arbitrary orientation of the parametric model presented in Section 2.3.4. The central star is placed at the origin. The outer disk lies in the x-y plane. The angle α is the relative inclination between the midplane of the outer disk and the plane of the inner disk. The dust mass density distribution of the inner disk and outer disk sections are rendered in false color. The gap is shown devoid of material for simplicity. The inner disk is scaled up in size and density for better visualisation.

We assume that the small grains that account for the bulk of the near-IR opacity approximately follow the gas background, and we define an axisymmetric gas distribution with a rounded disk wall [85, 103] described by the following surface density:

$$\bar{\Sigma}_g(r < r_c) = \Sigma_c \left(\frac{r}{r_c}\right)^{-\gamma} \exp\left[-\left(\frac{1 - r/r_c}{w}\right)^3\right], \tag{1.1}$$

$$\bar{\Sigma}_g(r \geq r_c) = \Sigma_c \left(\frac{r}{r_c}\right)^{-\gamma}, \tag{1.2}$$

where $\gamma = 6$, $w = 0.1$ and $r_c = 148.0$ au. Then we modulate this distribution to create a maximum gas pressure in azimuth, which is described by the following equations:

$$\Sigma_g(r, \phi) = \bar{\Sigma}_g(r)\left[1 + A(r)\sin\left(\phi + \frac{\pi}{2}\right)\right], \tag{1.3}$$

$$A(r) = \frac{c-1}{c+1}\exp\left[-\frac{(r - R_s)^2}{2H^2}\right], \tag{1.4}$$

with $R_s = 148$ au and where the azimuthal contrast in surface density is set to $c = 10.0$. The volume density follows with a standard vertical Gaussian distribution:

$$\rho_g(r, z, \phi) = \frac{\Sigma_g(r, \phi)}{\sqrt{2\pi}H}\exp\left[-\frac{z^2}{2H^2}\right], \tag{1.5}$$

with $H(r) = 20.0\,(r/(130\text{ au}))^{1.17}$. The exact value of this flaring exponent is not well constrained.

This parametric model also includes the effect of dust trapping, following the procedure described in [15] and [112]. However, the bulk of the opacity in H-band is driven by particles well below the sizes required for efficient aerodynamic coupling, and so the effects of dust trapping in the outer disk are not relevant for this chapter. The runs detailed in Section 1.3 confirm that the outer disk is optically thick at H-band and that the scattered light does not trace the crescent shape seen in the sub-mm.

1.2.2 Emergent intensities

We use RADMC3D[1] for radiative transfer computations [43, version 0.38,]. Scattering and polarization for last scattering are treated with scattering matrices for our different dust species, each one with a power law distribution in grain sizes with exponent -3.5. To compute the full dust opacity and scattering matrices we made use of complementary codes in RADMC3D for "Mie solutions" to scattering by homogeneous spheres [16]. We used the optical constant tables for amorphous carbon grains from [83], and for silicate grains we used [61].

We implemented our model in RADMC3D using spherical coordinates, with regular spacing for the azimuthal angle, and logarithmic spacing in radius and colatitude (polar coordinate). Thus, the grid is naturally refined near the inner disk and the midplane. The radial grid is additionally refined as it approaches the inner wall of the outer disk (near 140 au) to ensure a gradual transition from the optically thin gap to the optically thick outer disk. We used 10^6 cells in total, half of them covering the inner disk and gap, and the rest sampling the outer disk. The number of points in the radial, azimuthal and polar grid meshes is 100 each.

The Eastern side is probably the far side since it is broader and brighter in the thermal IR [49]. This orientation also implies that the observed IR spiral pattern is consistently trailing [7, 21, 22, 50], even in their molecular-line extensions into the outer disk [33]. Hence we calculated the synthetic H-band images by inclining the system at 24 deg with respect to the plane of the sky[2], along a position angle (PA) of –20 deg.

1.3 Results

In order to constrain the PA of the inner disk and α, its inclination with respect to the outer disk, we studied different orientations while trying to reproduce the shape and position of the nulls seen in scattered and polarized light. In Fig. 1.2 we summarize the radiative transfer predictions of 5 different configurations. PAs much different from -8 are ruled out,

[1] http://www.ita.uni-heidelberg.de/ dullemond/software/radmc-3d/

[2] the outer disk defines the plane of the system

as even a PA of 0 (see Fig. 1.2e) displaces the southern shadow so that it is inconsistent with the observations. In parallel, for low and negative α, the inclination and orientation of the shadows do not fit the shape of the nulls (see Fig. 1.2c&f). A qualitative match with the observations is obtained with an inner disk inclined at $\alpha = 70$ deg relative to the outer disk, and along a PA of -8deg (Fig. 1.2b). We can rule out configurations with PAs beyond 10 deg of -8 deg, so that the 1 σ error bar is about 5 deg. Likewise, the relative inclination is constrained within 60 to 80 deg, so that the 1 σ error is also $\sim$5 deg.

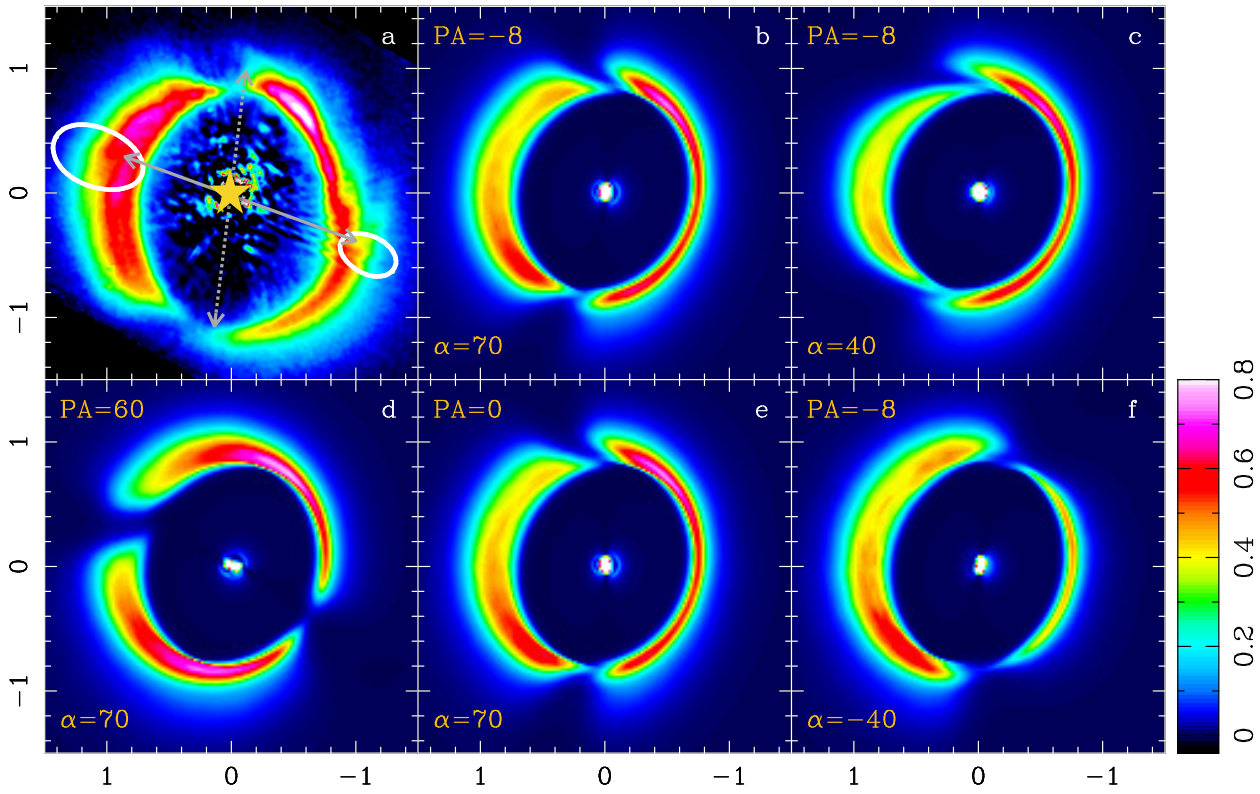

Figure 1.2: Impact of the inner disk orientation on the H-band light scattered off the outer disk. **a:** NACO-PDI H-band image from [7], compared with the $C^{18}O$(2-1) emission at systemic velocity from [108]. The $C^{18}O$(2-1) emission, represented here as one white contour at 0.75 maximum, shows that the position angle (PA) of the outer disk is at -20 deg East of North, and perpendicular to the solid gray double-arrow, while the position angle of the intensity nulls is indicated by the dashed double-arrow (-8 deg). **b-f:** Radiative transfer prediction for polarized intensity in H-band, for different inner disk PAs (indicated in degrees on the plots), and for different relative inclinations α between the inner and the outer disks. The $x-$ and $y-$ axis indicate offset along RA and DEC, in arcsec.

An inner disk orientation along a PA of $\sim$60° has been proposed previously [114], based on long-slit spectroscopy of the CO 4.67 μm line, along with a purely Keplerian disk model. However, as illustrated in Fig. 1.2d, such an orientation can be discarded from the H-band imaging. It is possible that non-Keplerian kinematics may have biased the orientation inferred from the ro-vibrational CO.

It is interesting that our models predict a peak $H-$band intensity at the same position as in the observations, at $\sim$1.5h (North-North-West). However, the second peak in the PDI

image to the North-East does not coincide with our radiative transfer predictions. This can be due to an effect of fine structure in the outer disk, or to deviations from a perfect ring, or to the stellar offset from the center of the cavity. These details are beyond the scope of our model.

The width of the shadows in the outer disk is dominated by the scale height of the inner disk, as it covers a wider solid angle of the star. A more detailed study could lead to a better constraint on the aspect ratio and flaring of the inner disk.

1.3.1 Comparison with ALMA band 7 image

Recent ALMA images at 345 GHz showed that the dust continuum emission of the outer disk is highly asymmetric [25, 51], with an azimuthal modulation close to an azimuthal wavenumber $m = 1$. The peak intensity is located to the north-east of the star. New ALMA data at 700 GHz shows a similar structure with a higher resolution [26], however along the crescent morphology two peak intensities stand out with a decrement between them. This decrement can be understood as a temperature decrement as it is located in the shadowed region of the outer disk. Moreover, the cooling time scales in the outer disk is shorter than crossing time along a shadow, hence the gas and dust have enough time to cool down under the shadows. In Figure 1.3 we present the new ALMA band 9 image together with the predicted intensities from our warped disk model. Our model reproduces the two peak intensity structure without the need of reducing the amount of dust in the decrement.

Finally in Figure 1.4 we present the HD 142527 dereddened SED and the disk model SED. The model matches roughly the observations from the visual to the radio.

1.4 Discussion

Warped disks are found in varied astrophysical contexts. Galactic warps may be due to a misalignment between a galaxy's angular momentum and its surrounding dark matter halo [14] or by tidal encounters with nearby galaxies [66]. Previous studies on HD 142527 also propose that the two-armed spirals in the outer disk might be indicative of a recent close stellar encounter [33, 115]. Although a flyby could also explain the tilt between the inner and outer disks, no partner for such a stellar encounter has been identified.

In the prototypical T-Tauri disk TW Hya, it was proposed a warp to understand the sinusoidal ($m = 1$) azimuthal modulation seen in *HST* images, as well as features of the CO gas kinematics of the inner most regions [122]. The same study found that a standard Keplerian disk model was unable to account for the CO line wings and spatially resolved emission near the central star, and explored 3 possible interpretations to account for the observed kinematics: 1) scaling up the temperature by a factor of three inside the cavity; 2) allowing super-Keplerian tangential velocities near the star, and 3) invoking a warped disk model in which the line-of-sight disk inclination increases towards the star.

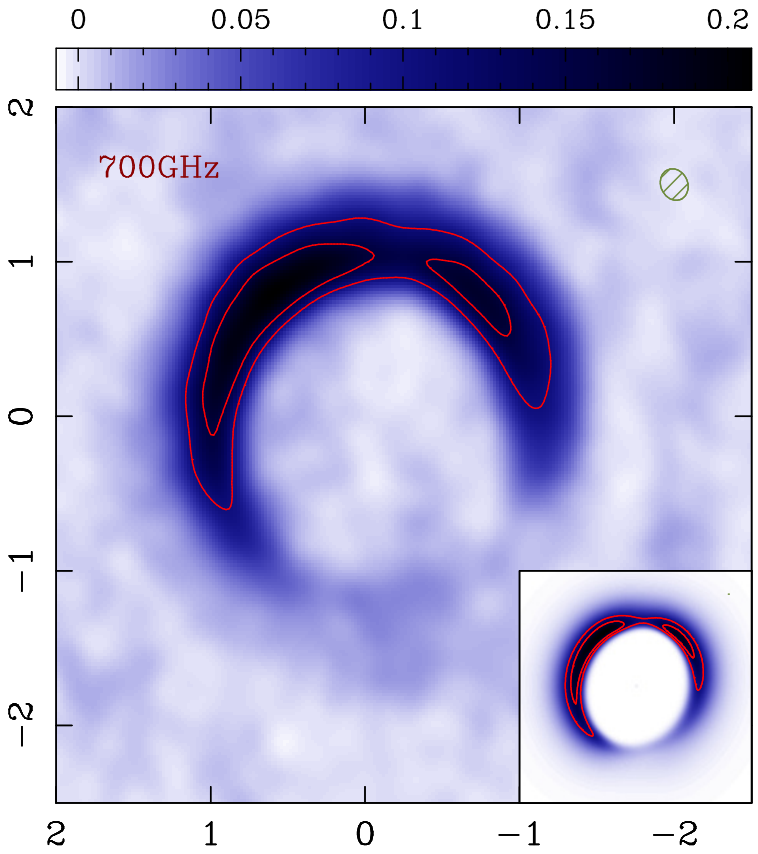

Figure 1.3: ALMA band 9 observations of HD 142527, and comparison with synthetic predictions [26]. $x-$ and $y-$axes indicate angular offset in arcsec along right-ascension (RA) and declination (Dec) relative to the stellar position, at the origin of coordinates. The color scale shows a restored image of the ALMA band 9 at 700 GHz, with contours at 0.5 and 0.75 times the peak intensity. The wedge indicates specific intensity in Jy beam^{-1}, with a beam of $0.21'' \times 0.17''$ (the beam ellipse is shown on the upper right corner). The inset shows emergent intensities predicted from the dust trap model, including the impact on grain temperatures due to shadowing from a tilted inner disk. Contours are at 0.5 and 0.75 times the peak, no smoothing has been applied. The side of the inset corresponds to $3.5''$.

Dynamical interaction between circumstellar disks and (proto)planets or sub-stellar companions may lead to warps [102]. In the β Pictoris debris disk, the inner disk warp may have been dynamically induced by β Pic b [38], whose orbit is found to be aligned with the inclined warped component [32, 80].

A warped inner disk in HD 142527 bears consequences on the physical conditions in the outer disk. The shadowed regions in the outer disk along the inner disk midplane can be diagnosed in terms of temperature decrements in sub-mm continuum imaging [26]. In addition the shadows in the outer disk might have an impact on the hydrodynamics as they could be treated as temperature perturbations. These perturbation could produce spiral waves, explaining the spiral arms seen in the outer disk and the no detection of planets launching these spirals. A question arises as to the origin of this warped disk, which is probably driven by the low-mass companion [13, 36, 121], although it could also be linked with the disk-envelope interaction leading to the formation of the binary in the class I stage.

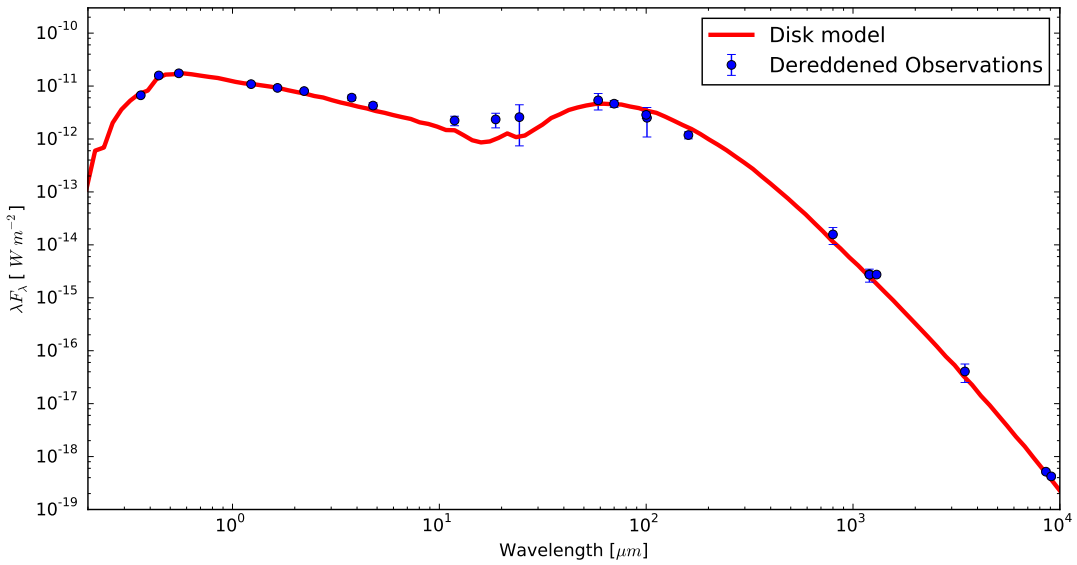

Figure 1.4: Dereddened SED of HD 142527 (blue dots) compared with the model (red line). We deredden the observations assuming a visual extinction A_V =0.6 [137] and an total-to-selective extinction ratio of R_V =3.1. The errorbars represent 3 σ errors.

Since there is no apparent displacement of the shadows by comparing the NICI images, acquired in June 2011, with the NACO PDI from July 2012, we can exclude the possibility that the inner tilt is precessing at a rate faster than $\sim$10 deg yr^{-1}. Likewise, we can discard shadows cast by compact concentrations of material in the very closest vicinity of the star.

1.5 Conclusions

The detailed scattered light images of HD 142527 available in the literature, coupled with state-of-the-art radiative transfer tools, have allowed us to conclude on the three-dimensional structure of the system by levering on the inner disk shadows. The inner regions turn out to be warped, such that its inclination relative to the outer disk is 70$\pm$5 deg, and its PA is -8 ± 5 deg.

Moreover, the two peak intensity structure seen in the new ALMA image can be understood as a single crescent split by a temperature decrement caused by the inner disk shadows. This region is colder due to the missing stellar heating compared to its immediate surroundings. This is well reproduced by our synthetic model and brings an independent proof to our warped disk model.

This finding poses a challenge to understand the dynamics of the HD 142527 system, and is an invitation to interpret scattered light images of gapped protoplanetary disks from the perspective of inner warp shadows.

Chapter 2

Compact dust concentration in the MWC 758 protoplanetary disk

2.1 Introduction

In this chapter we study the transition disk around the Herbig Ae star MWC 758 (HD 36112). The main parameters for this system are given in Table 2.1. The central star is 3.7 ± 2.0 Myr old [98], and optical spectroscopy reveals variable profiles suggesting jet-like inhomogeneities at different distances from the star [12]. The revised *Hipparcos* parallax data put the star at a distance of 279^{+94}_{-58} pc [136], although most previous studies use the old *Hipparcos* estimated distance of 200^{+60}_{-40} pc [134]. From ^{12}CO(3-2) kinematics, it was determined a stellar mass of $2.0 \pm 0.2 M_{\odot}$ and a disk orientation with an inclination (i) of $21 \pm 2^{\circ}$ and a position angle (PA) of $65 \pm 7^{\circ}$, all consistent with Keplerian rotation [69]. Despite its bright infrared excess, a cavity of $0.37''$ (73 astronomical units (au) at 200 pc) has been inferred from dust millimeter emission suggesting a depletion of millimeter grains in the inner regions of the disk possibly due to the presence of a low-mass companion within a radius of 30 au [4, 69]. In addition, the SED shows a 10 μm dip consistent with a pre-transitional disk [55], but with a strong near-infrared emission coming from sub-au scales observed with VLTI [68].

The disk structure shows deviations from an axisymmetric disk. Spiral arms are detected from near-IR scattered light and thermal emission images extending from the sub-millimeter cavity to the outer disk [11, 55]. The drop in the polarised intensity beyond the spiral arms can be interpreted as a shadowing effect by the arms, as the disk extends farther out in the millimeter. In addition, at millimeter wavelengths a peak intensity in the dust continuum has been detected to the north-west of the central star after subtraction of a best-fit axisymmetric model, suggesting an asymmetry in the millimeter dust grain distribution in the outer parts of the disk [69]. Moreover, in the same study, asymmetries in CO emission were observed that could be due to a warped optically thick inner disk [69], similar to the case of HD 142527 [94]. If the southern spiral arm is trailing, the disk is rotating with a clockwise direction in the plane of the sky, where the north side of the disk is the nearest.

In this paper we analyse new VLA Ka & Ku observations and we compare with ALMA

archival data to study the distribution of dust grains and search for evidence of grain size segregation due to dust trapping. In Section 2.2 we describe the data and imaging. In Section 2.3 we investigate the origin of the VLA Ka & Ku emission, comparing with archival ALMA and SPHERE data, and we describe a parametric vortex model that reproduces the basic morphology seen in the VLA and ALMA images, and the SED. In Section 2.4 we discuss about the origin of the asymmetries. Finally in Section 2.5 we summarize the main conclusions of this work.

Table 2.1: Main parameters of MWC 758.

Parameter	Value	Reference
RA (J2000)	$05^h\ 30^m\ 27.530^s$	[136]
DEC (J2000)	$+25^\circ\ 19'\ 57.082''$	[136]
Age	3.7 ± 2.0 Myr	[98]
Stellar Mass	$2.0 \pm 0.2 M_\odot$	[69]
V	8.27	[64]
$B-V$	0.3	[64]
H	6.56	[37]
Distance	279^{+94}_{-58} pc	[136]
Disk inclination	$21 \pm 2^\circ$	[69]
Disk PA	$65 \pm 7^\circ$	[69]

2.2 Observations and Imaging

In this section we describe the observations and imaging of the VLA Ka (∼33 GHz) & Ku (∼15 GHz) and ALMA Band 7 (∼337 GHz) data. The image synthesis was carried out using a non-parametric least-squares modeling technique with a regularization term called entropy from the family of maximum entropy methods (MEM). We call the whole algorithm and code *uvmem* and the resulting deconvolved model images are labelled as 'MEM model'. It is possible to characterize the resolution level with a synthetic beam derived from the response of the algorithm to a point source with the same noise level as the observations. The MEM synthetic beam is usually finer than the standard Clean beam with natural or *briggs* weighting

The deconvolved model images are 'restored' by adding the dirty map of the residuals of *uvmem* and convolving with a Clean beam characteristic of natural or *briggs* weighting. These images can be compared with Clean images and are labelled as 'restored images'.

2.2.1 VLA

The VLA observations form part of the project VLA 13B-273. The MWC 758 observations were acquired on 6 runs: 3 nights in October and November of 2013 in Ka band and another 3 nights in January of 2014 in Ku band. In Ka band the target was observed in B 0 configuration with minimum and maximum projected baselines of 190 m and 10.5 km, while in Ku band it

was observed in BnA 0 configuration with minimum and maximum projected baselines of 80 m and 23 km. The array included 27 antennas of 25 m diameter, and the total integration time on source was 1h 21min in each band.

For Ka band, the VLA correlator was configured to produce 64 spectral windows from 28.976 GHz to 37.024 GHz, with a spectral window bandwidth of 128 MHz, each divided into 64 channels to study the continuum emission with a resolution of 2 MHz. In Ku band, the correlator was configured similarly with 64 spectral windows covering from 11.976 GHz to 18.224 GHz, each divided into 64 channels of 2 MHz width.

In all the observations, 3c138 was used as primary flux calibrator, while J0547+2721 was used as phase calibrator with 4 observations of 1min 30s between the target observations of 9 min. After looking at the resulting images from each run to check the quality of the data, we excluded one of the three observing runs with Ka band.

VLA images

In Figure 2.1 we present the restored VLA Ka image and restored image after subtracting the central component with a point source fit to the visibilities. The Ka image presents a noise level (σ) of 6.6 μJy beam^{-1} and the beam size is $0.23'' \times 0.22''$. Two bright compact regions separated by $0.5''$ stand out from some extended emission, which is not very well resolved due to low signal-to-noise. The southern compact emission has a peak intensity of 63.0 μJy beam^{-1} and is located at the position where the star is expected according to the stellar coordinates and proper motion [110]. The other compact emission is 44.0 μJy beam^{-1} and is located to the north-west of the star, where previous SMA and CARMA observations found an intensity maximum at millimeter wavelengths [69]. To the south of the star there is also disk emission with a peak intensity of 30.0 μJy beam^{-1}, slightly higher than 4σ. This probably correspond to dust thermal emission from the disk and puts an upper limit to the disk emission at this frequency. However, the morphology of this emission is hard to elucidate given the noise levels and resolution. The northern clump is separated from the star by $0.5''$, which at a distance of $\sim$280 pc translates to a de-projected radius of 150 au in the disk plane. The total disk flux is $252 \pm 34\mu$Jy.

The Ku data only shows compact emission coming from the star location with a total flux of 67.1$\pm$7.7 μJy and an image noise level of 4.1 μJy beam^{-1}. The synthetic beam of this observation corresponding to natural weights has a size of $0.56'' \times 0.18''$. We are not showing the Ku image because it is featureless and only shows a point source at the stellar position.

Flux loss

We neglect flux loss in the VLA data. To study this possibility in the VLA Ka observations due to missing baseline spacing and limited u-v coverage, we simulated observations using a model image of the disk at 337 GHz and the VLA Ka u-v coverage (the model is described in Section 2.3.4). We scaled the intensity levels of the model image to have a simulated peak intensity equal to the Ka peak intensity. Gaussian noise was added to the model visibilities.

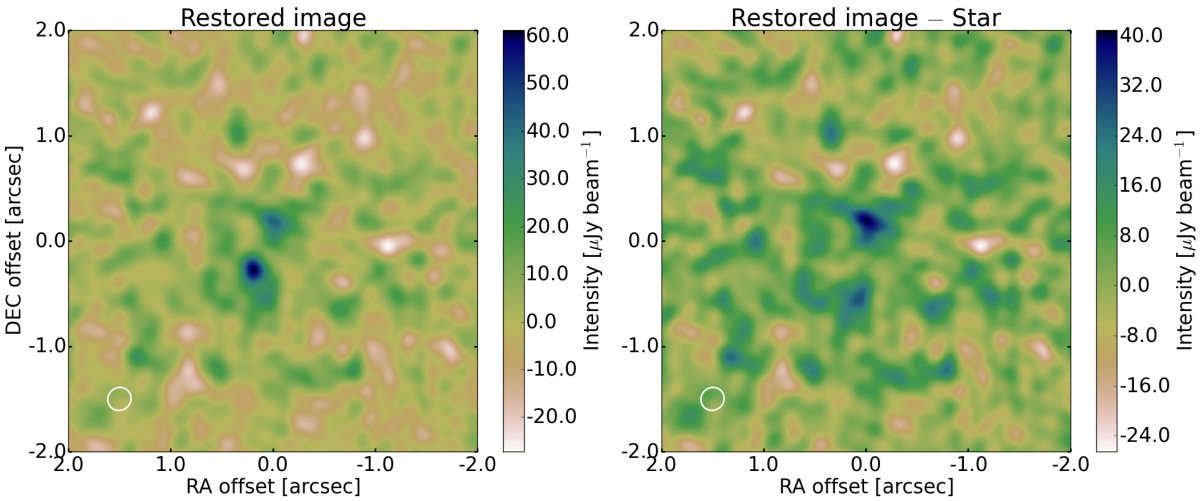

Figure 2.1: Restored VLA Ka ($\sim$ 33 GHz) images. Left panel: restored image. Right panel: restored image after subtracting the star. The beam size in the Ka images is $0.23'' \times 0.22''$ and is represented by a white ellipse in both images. The x & y axes indicate the offset in RA and DEC in arcsec, i.e. north is up and west is right.

The final simulated image has a total flux of 620±27 inside a circumference of radius 0.9, centered at the stellar position. This is consistent with the model flux of 609 Jy within the estimated errors.

2.2.2 ALMA

To study the disk continuum emission at millimeter wavelengths we made use of ALMA archival data in Band 7 of MWC 758 from the project 2011.0.00320.S [31]. The observations were conducted over two nights in August and October of 2012. The ALMA correlator was set in Frequency Division Mode (FDM) to provide 4 spectral windows divided in 384 channels, centered at 337.773 GHz with a total bandwidth of 234.363 MHz, 344.469 GHz with a total bandwidth of 234.363 MHz, 332.488 GHZ with a total bandwidth of 233.143 MHz and at 330.565 GHz with a total bandwidth of 233.143 MHz. The observations were carried with 29 antennas of 12 meter diameter. The minimum and maximum projected baselines were 15 and 375 m and the total time on source was 12 min. We flagged the lines CO J =3-2 (337.79599 GHz) and ^{13}CO J =3-2 (330.58797 GHz) to study the dust continuum emission.

In Figure 2.2 we present the ALMA MEM image using *uvmem* and a restored image that can be compared to a Clean image. The model image has an approximate resolution of $0.31'' \times 0.18''$, derived from the response to a point source. The restored image was produced by convolving with a Clean beam of size $0.64'' \times 0.40''$ characteristic of *briggs* weighting to achieve a better resolution. In the restored image, the noise level is 1.3 mJy beam^{-1}, while the peak intensity is 55.0 mJy beam $^{-1}$. The total flux is 210 ± 5 mJy.

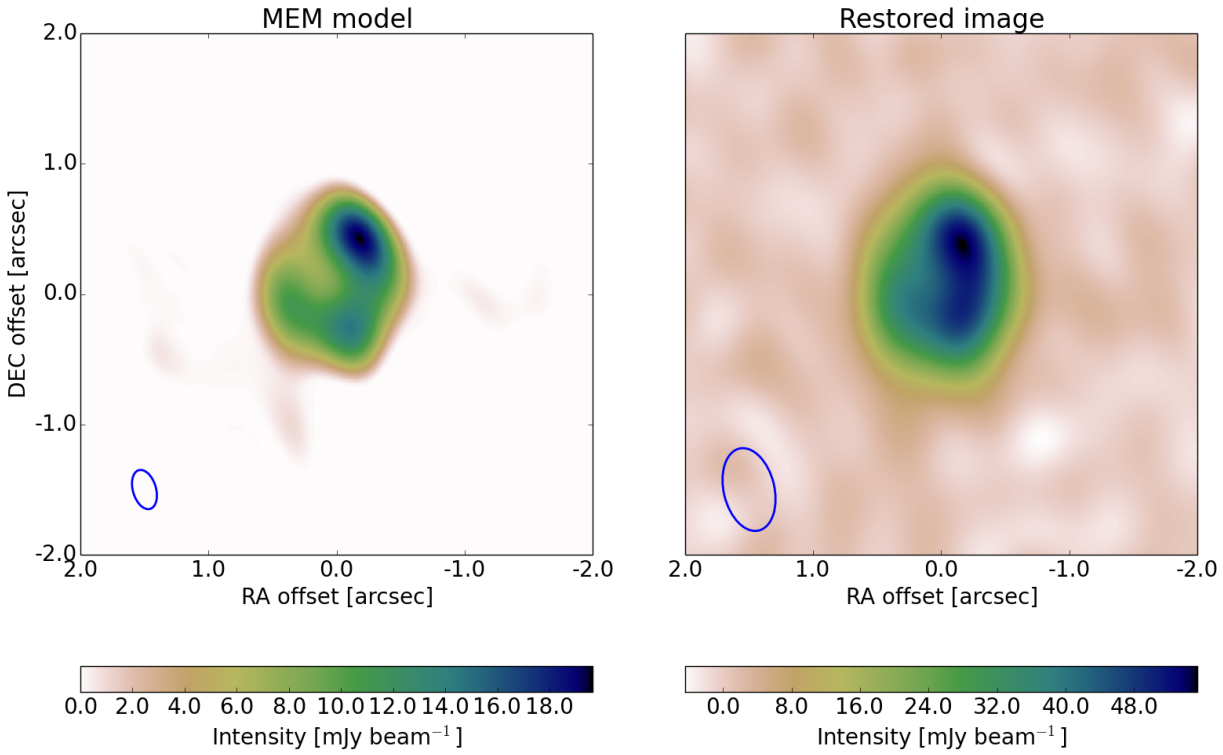

Figure 2.2: ALMA maps at 337 GHz (Band 7). Left panel: MEM non-parametric model (regularized with the maximum entropy method) with a synthetic beam of $0.31'' \times 0.18''$. Right panel: Restored image adding residuals and convolving with a Clean beam corresponding to *briggs* weighting (0.64×0.40). The respective beams are represented by blue ellipses. The star position is expected to be at the center of the image. The x & y axes indicate the offset in RA and DEC in arcsec, i.e. north is up and west is right.

2.3 Analysis

The VLA Ka and ALMA maps show that the disk of MWC 758 is very far from an axisymmetric disk. The disk shows a peak of intensity to the north-west side of the disk, centered at a distance of $0.5''$ from the star, consistent with previous millimeter observations [69]. In both ALMA maps and more evident in the MEM model, a local intensity minimum appears at the center of the disk, confirming the presence of a cavity of millimeter grains. Unlike the case of HD 142527 and IRS 48, the maximum and minimum of intensity are not opposite in azimuth (azimuthal wavenumber m = 1) [24, 51, 135]. Moreover, a second maximum in azimuth appears in the MEM model to the south-west of the star, which translates to an azimuthal extension to the south of the northern intensity maximum in the restored image.

2.3.1 Spectral trends

To investigate the origin of the emission in the VLA maps, it is useful to compute the intra-band and inter-band spectral indexes, defined as $\alpha_{\nu_1}^{\nu_2} = \log(I_2/I_1)/\log(\nu_2/\nu_1)$. The Ka-Ku

inter-band spectral index (α_{15}^{33}) of the emission coming from the stellar location is 0.36 ± 0.20, while the Ku intra band spectral index is $\alpha_{15} = 0.8 \pm 0.6$, computed from a point source fit to the Ku data at the different channels. Both values are consistent with free-free emission from the central star associated with a stellar wind or stellar accretion. Assuming a spectral index between 0.5 and 1.0 from free-free emission and the VLA flux level at 33 GHz, we expect emission levels of 0.2-0.7 mJy beam^{-1} at 337 GHz, well below the disk emission and the noise level reached in the ALMA data. Similar unresolved emission has been detected with ATCA observation at the location of the central star in HD 142527 with a slightly higher spectral index of 1.0±0.2 [26].

On the other hand, the northern compact emission has an inter-band spectral index of $\alpha_{Ka}^{B7} = 3.1 \pm 0.1$ when we compare with the intensity maximum of the restored ALMA image. Using α_{Ka}^{B7} the predicted flux of the northern clump at 15 GHz is ∼6.0 μJy, slightly above the noise level of the Ku data.

Given the unknown temperatures, the uncertainties in the clump flux, the non detection at 15 GHz, and the lack of spatial resolution in the ALMA data, it is not possible to conclude on the spectral index β for an optical depth power law $\tau(\nu) \propto \nu^{\beta}$, preventing us from studying a direct relation between the observations and a dust size distribution in the northern clump. Additional observations with similar resolution levels are necessary to derive a β index to directly study the dust size distribution in the clump. However, in Section 2.3.4 we implement a simple parametric vortex model for the disk that reproduces the SED and morphology of the VLA and ALMA maps. We use this model to interpret the VLA clump in Section 2.3.4.

2.3.2 Comparison between ALMA and VLA Ka maps

In Figure 2.3, we present an overlay between the restored VLA Ka image and the ALMA band 7 MEM model. The VLA Ka northern peak intensity matches the location of the ALMA band 7 maximum. At 337 GHz we expect that most of the emission comes from ∼millimeter-sized grains. If this intensity maximum is tracing a maximum in the dust density distribution of millimeter-sized grains, the VLA and ALMA maxima could be due to dust grains being trapped in a pressure maximum of the gas. In the dust trap scenario, we would expect to observe at centimeter wavelengths a higher contrast between the intensity maximum and the rest of the disk and a more compact emission, probing the distribution of centimeter-sized grains that are more easily trapped in gas pressure maxima. However, the ALMA maps are not as well spatially resolved as the VLA Ka image due to differences in the u-v coverage. In Sec. 2.3.3 we compare both datasets at the same resolution level.

Figure 2.3 also shows disk emission to the south of the stellar position in the VLA Ka map that matches a second peak intensity in the ALMA MEM model. This peak is closer in than the northern clump, at an angular distance of $0.3''$. However this local maximum disappears in the restored ALMA image due to the larger Clean beam.

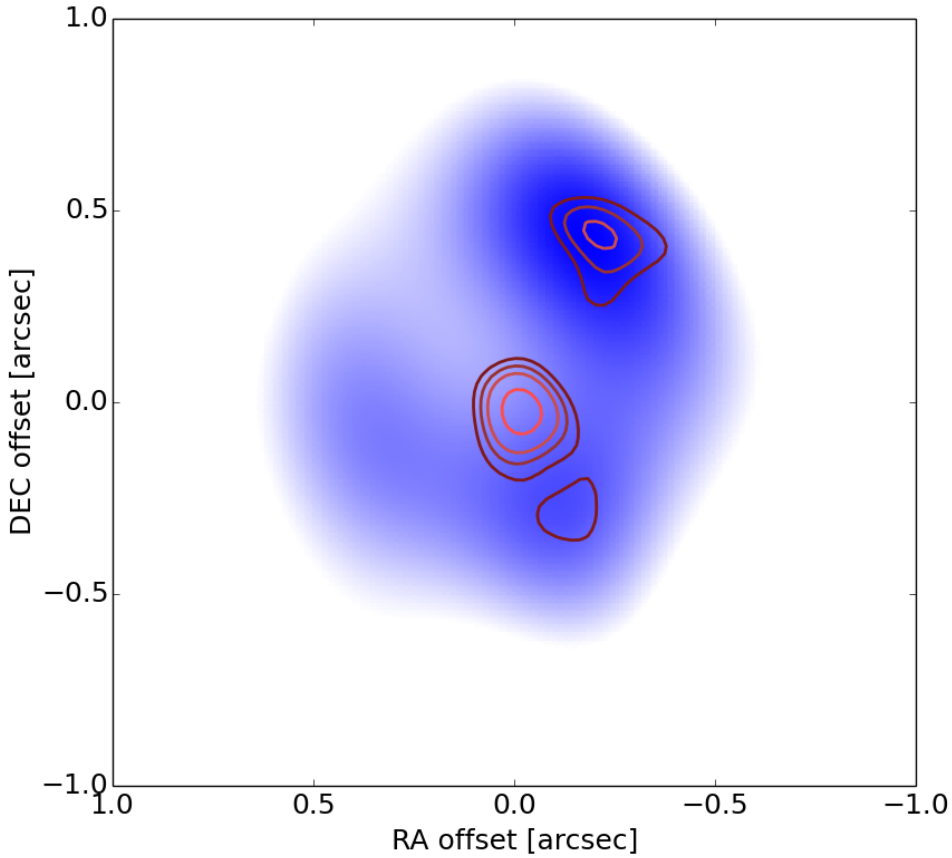

Figure 2.3: ALMA-VLA overlay. In blue the ALMA band 7 MEM model in an arbitrary color scale, while in red the restored VLA Ka image contours set at arbitrary levels to highlight the morphology (the lowest contour level is 4.2 σ). The x & y axes indicate the offset in RA and DEC in arcsec, i.e. north is up and west is right.

2.3.3 ALMA and VLA Ka map at the same resolution level

To bring both datasets to comparable resolutions, we convolved the restored VLA Ka image with the ALMA Clean synthetic beam of size $0.64'' \times 0.40''$ after subtracting the star. We call this map the degraded VLA image. In Figure 2.4 we show the contour levels 0.6, 0.75, 0.85 and 0.93 peak intensity of the degraded VLA and restored ALMA images. The degraded VLA image presents a morphology similar to the ALMA MEM model with two peak intensities: to the north-west and south of the star (see Fig. 2.2). The northern clump in the degraded VLA image is still more compact than in the restored ALMA image, with a larger contrast. The solid angle inside the 0.85 intensity maximum contour in the degraded VLA image is 0.09 arcsec^2, while it is 0.23 arcsec^2 in the ALMA map. This result strongly supports the dust trap interpretation, finding that the bigger grains traced at centimeter wavelengths are more concentrated around this pressure maximum.

The peak intensity to the south of the star in the restored VLA Ka image remains after star subtraction and convolution with the ALMA beam, with a morphology similar to that observed in the ALMA MEM model. The nature of this compact emission is not clear as it

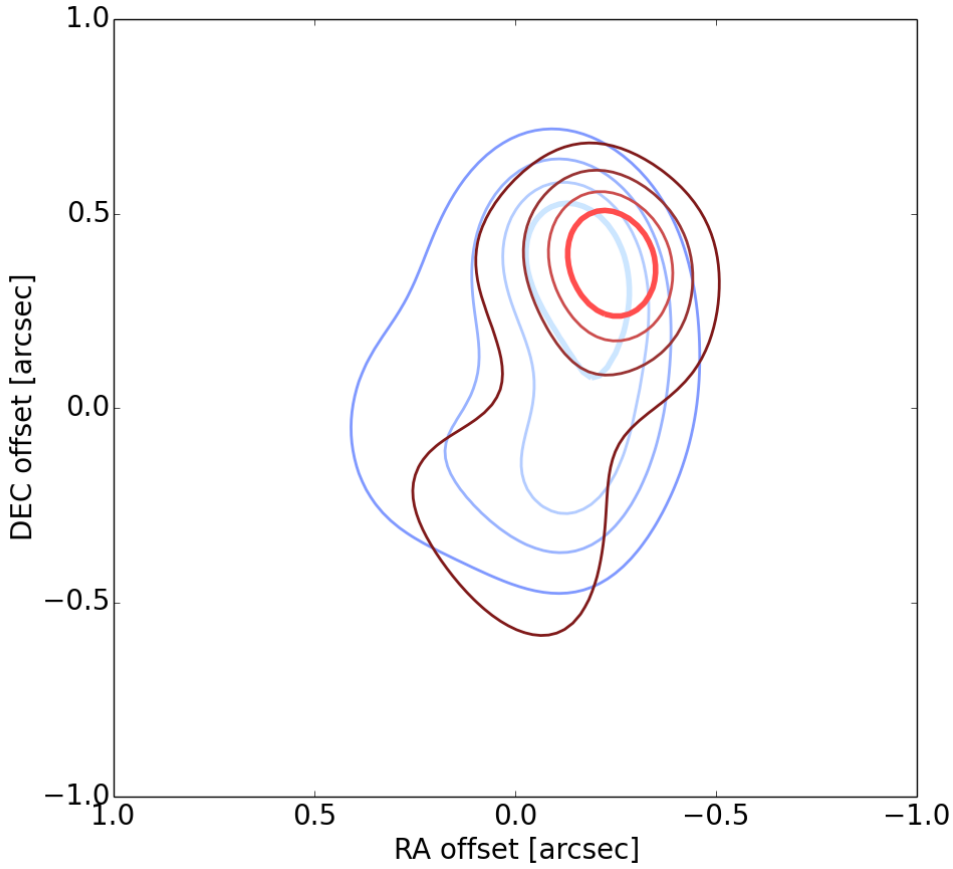

Figure 2.4: ALMA-VLA map contours overlay. Blue contours: ALMA Band 7 restored image. Red contours: degraded VLA image (restored image after subtracting the star and convolving with the ALMA beam). The contour levels are 0.6, 0.75, 0.85 and 0.93 times the peak intensity of each map. The contour levels are arbitrary to emphasise the disk morphology. The lowest contour level of the VLA map represents 3σ at this resolution. The thick red and blue lines represent the 0.93 peak intensity level. The x & y axes indicate the offset in RA and DEC in arcsec, i.e. north is up and west is right.

is just $\sim$4 times the noise level in the restored VLA Ka image. At the ALMA resolution the cavity is hard to distinguish, although the peak intensity is offset from the stellar position in both maps, suggesting a cavity depleted of big grains.

To confirm the dust trap interpretation, ALMA observations in extended configuration are required to resolve the disk with a similar or finer resolution than the VLA Ka observations. Deeper VLA observations are also necessary to detect the rest of the disk.

2.3.4 Parametric non-axisymmetric model

We develop a parametric non-axisymmetric disk model, inspired by the steady state vortex solution to the gas and dust distribution described in Lyra & Lin (2013) [89, hereafter L^{2}13]. The aim is to reproduce part of the morphology seen in the ALMA and VLA maps, and the

global SED. The model consists of a central star surrounded by a disk of gas and dust. We model the star using a Kurucz template spectrum [29] with a temperature of 8250 K and a stellar radius of 2.6 $R_\odot$, to fit the SED in the optical with a visual extinction of 0.22 [134]. We define two distinct disk zones (see Table 2.2):

1. A dusty inner disk with small grain sizes ranging from 0.1 to 1 μm, composed of amorphous carbon and silicate grains to reproduce the NIR excess.
2. A non-axisymmetric outer disk composed of amorphous carbon and silicate grains to reproduce part of the disk morphology seen in the VLA and ALMA images, and the photometry from the SED in the FIR and radio.

Table 2.2: Disk parameters

Parameter	Inner disk	Outer Disk
$r_{\rm min}$ [au]	0.2	20.0
$r_{\rm max}$ [au]	80.0	300.0
$\Sigma(r)$	$\Sigma_c \left(\frac{r}{r_c}\right)^{-0.5}$	Eq. 2.11
$H(r)$ [au]	$0.2\left(\frac{r}{1.0\ \rm au}\right)^{1.1}$	$19.0\left(\frac{r}{100.0\ \rm au}\right)$
$M_{\rm d}$[1] [$M_\odot$]	5.0×10^{-8}	$7.1{\times}10^{4}$
Mass fraction in Silicates	0.9	0.48
a_{min} [μm]	0.1	1.0
a_{max} [μm]	1.0	$5{\times}10^{3}$

The total gas mass in the disk is 0.1 M_*. The outer disk incorporates an analytic prescription for a steady state vortex defined for both gas and dust distribution, based on the work of L^{2}13. We first define an axisymmetric gas background inspired by the surface density distribution used in previous studies [69], and following the solution for the surface density of a viscous Keplerian disk [88]

$$\Sigma_b(r) = \Sigma_c \left(\frac{r}{r_c}\right)^{-\gamma} \exp\left(-\frac{1}{2(2-\gamma)}\left[\left(\frac{r}{r_c}\right)^{2-\gamma} - 1\right]\right), \tag{2.1}$$

$$\rho_b(r,z,S) = \frac{\Sigma_b(r)\sqrt{S+1}}{\sqrt{2\pi}H} \exp\left[-\frac{z^2}{2H^2}(S+1)\right], \tag{2.2}$$

where H is the scale height of the disk and S is defined as the ratio between the the Stokes number (St) and δ_t, a turbulent diffusion parameter that measures the strength of the turbulence in the disk. We assume a global δ_t in the disk for simplicity, although the turbulence in the core of the vortex can be driven by different mechanisms than in the rest of the disk. We set $r_c = 100.0$ au and $\gamma = -2.0$ to form an outer disk that matches the peak intensity and cavity in the ALMA observations, and the SED at long wavelengths. However, these parameters are not well constrained due to the lack of spatial resolution in the ALMA data and SED degeneracies.

We add the vortex steady state solution described by eq. 64 in L^{2}13 with a slight modification to include a global disk gas density field. We impose that the gas density described by the vortex solution has to match the gas background at the vortex boundary where the vortex

flow becomes supersonic with respect to the disk. This happens when a (defined in L^{2}13 as the axial elliptical coordinate corresponding to the vortex's semi-minor axis) is equal to $\frac{H}{\chi\omega_V}$, where χ is the vortex aspect ratio and $\omega_V = \Omega_V/\Omega$ is the dimensionless vortex frequency. Assuming the vertical dependence is the same inside and outside the vortex, we can focus only in the midplane. The density field inside the vortex can be written as

$$\rho(r,\phi) = c\rho_b \exp\left[-\left(\frac{(r-r_0)^2}{2H_v^2} + \frac{r_0^2(\phi-\phi_0)^2}{2H_v^2\chi^2}\right)\right], \tag{2.3}$$

where c is a constant determined by the condition that the vortex density field must match the background density field ρ_b at the vortex boundary. $H_v = H/(f(\chi)\sqrt{S+1})$ is the vortex scale length, where $f(\chi)$ is a scale function defined in L^{2}13 and is a function of χ. Defining

$$x = r - r_0, \tag{2.4}$$

$$y = r_0(\phi - \phi_0), \tag{2.5}$$

$$a = \sqrt{x^2 + \left(\frac{y}{\chi}\right)^2}, \tag{2.6}$$

Equation 2.3 translates into

$$\rho(a,S) = c\rho_b \exp\left[-\frac{a^2 f^2(\chi)}{2H^2}(S+1)\right] \tag{2.7}$$

and the condition can be written as

$$\rho_b = \rho(a = \frac{H}{\chi\omega_V}, S), \tag{2.8}$$

$$\rho_b = c\rho_b \exp\left[-\frac{f^2(\chi)}{\chi^2\omega_V^2}(S+1)\right], \tag{2.9}$$

finally obtaining $c = \exp\left[\frac{f^2(\chi)}{\chi^2\omega_V^2}(S+1)\right]$. Thus, the global solution is

$$\rho(r,\phi,z) = \rho_b(r,z)\max\left\{1,\ c\ \exp\left[-\frac{a^2 f^2(\chi)}{2H^2}(S+1)\right]\right\}. \tag{2.10}$$

A more realistic or smoother solution can be written as

$$\rho(r,\phi,z) = \rho_b(r,z)\left(1 + \ (c-1)\ \exp\left[-\frac{a^2 f^2(\chi)}{2H^2}(S+1)\right]\right), \tag{2.11}$$

and is valid for the gas ($S = 0$) and dust grains with a specific size a_s.

We set $\chi = 3$ and $\delta_t = 3 \times 10^{-3}$. To compute ω_V we use the Goodman-Narayan-Goldreich solution [54].

Using Eq. 2.11 and reasonable values for $\delta_t = 10^{-2} - 10^{-3}$, it is impossible to produce a vortex with the necessary contrast and size required to reproduce the asymmetry seen in the ALMA maps. To increase the contrast and vortex size, we artificially extend the

vortex steady state solution beyond its original boundary to obtain a better match with the observations (see Sec. 2.4 for a discussion on this). If we extend the vortex from its original boundary to $\frac{r_s H}{\chi \omega_V}$, c has to be redefined as $c = \exp\left[\frac{r_S^2 f^2(\chi)}{\chi^2 \omega_V^2}(S+1)\right]$ and the final density field is described by Eq. 2.11. We set $r_s = 2$ to have a good match between the restored ALMA image and the model image convolved with the synthetic ALMA beam (see Figures 2.2 and 2.5d).

We implement the model using 9 dust species in total: 2 dust species for the inner disk, representing silicates and amorphous carbon grains; 7 dust species for the outer disk, one accounting for small amorphous carbon grains (from 1 to 10 μm), while the others represent silicate grains from 1 μm to 5 mm with different spatial distributions set by Eq. 2.11. The opacities for each dust species in the model are computed using the 'Mie Theory' code written by Bohren & Huffman (1983) [16] considering a dust size distribution with a power law index of -3.5, and optical constants for amorphous carbon [83] and "Astronomical silicate" [40]. The emergent intensities from our model at different frequencies were computed using RADMC-3D version 0.39 [2] [44], using the Henyey & Greenstein parametrization of the phase function of scattering [62].

In Figure 2.5 we present the model images at 33 and 337 GHz at the top. The middle images show the simulated observations of the model images with the same u-v coverage and noise levels of the VLA Ka and ALMA observations. In addition, we present the model SED that matches roughly the observations. As expected from the vortex model, at long wavelengths the disk emission is concentrated in the pressure maximum as it traces the distributions of bigger grains which are highly trapped inside the vortex.

The simulated ALMA image shows a peak of intensity similar to the restored ALMA image, although the morphology is not exactly the same. Due to the lack of long baselines in the ALMA u-v coverage, the emission coming from the vortex position is spread over a larger solid angle, predicting higher disk emission in the north-east side of the disk, where the ALMA images show a decrement. Another interesting difference is the second intensity maximum seen in the ALMA MEM image, which appears as an extension to the south of the maximum in the restored image. This is not reproduced by our model and a second vortex would be needed to account for this emission. In Figure 2.6 we present the restored image from a simulated observation of a model with two vortices located at the position of the VLA northern and southern clumps. The southern extension of the peak intensity is naturally reproduced, and also the decrement at the north-east side of the disk due to the elongated beam. The VLA simulated observations show two clumps at the location of the VLA northern and southern clumps.

If the northern clump emission seen in MWC 758 in band 7 and Ka data is produced by a dust trap, it is a possible location for planetesimal and planetary core formation, as grains can grow faster and avoid the inward drift. From our model the dust temperature at the clump position is $\sim$30 K, but in the observations the brightness temperature of the clump at 33 GHz is 1.0 K. Thus it is highly unresolved or it is optically thin at this frequency. From our synthetic model, the inferred dust mass inside the vortex boundary is $\sim 30\ M_\oplus$, enough mass to form several planetesimals that could lead to the formation of a planetary core of a

[2] http://www.ita.uni-heidelberg.de/~dullemond/software/radmc-3d/

gas giant. However, grain porosity is not included in our model, thus this inferred mass is probably higher than the real value.

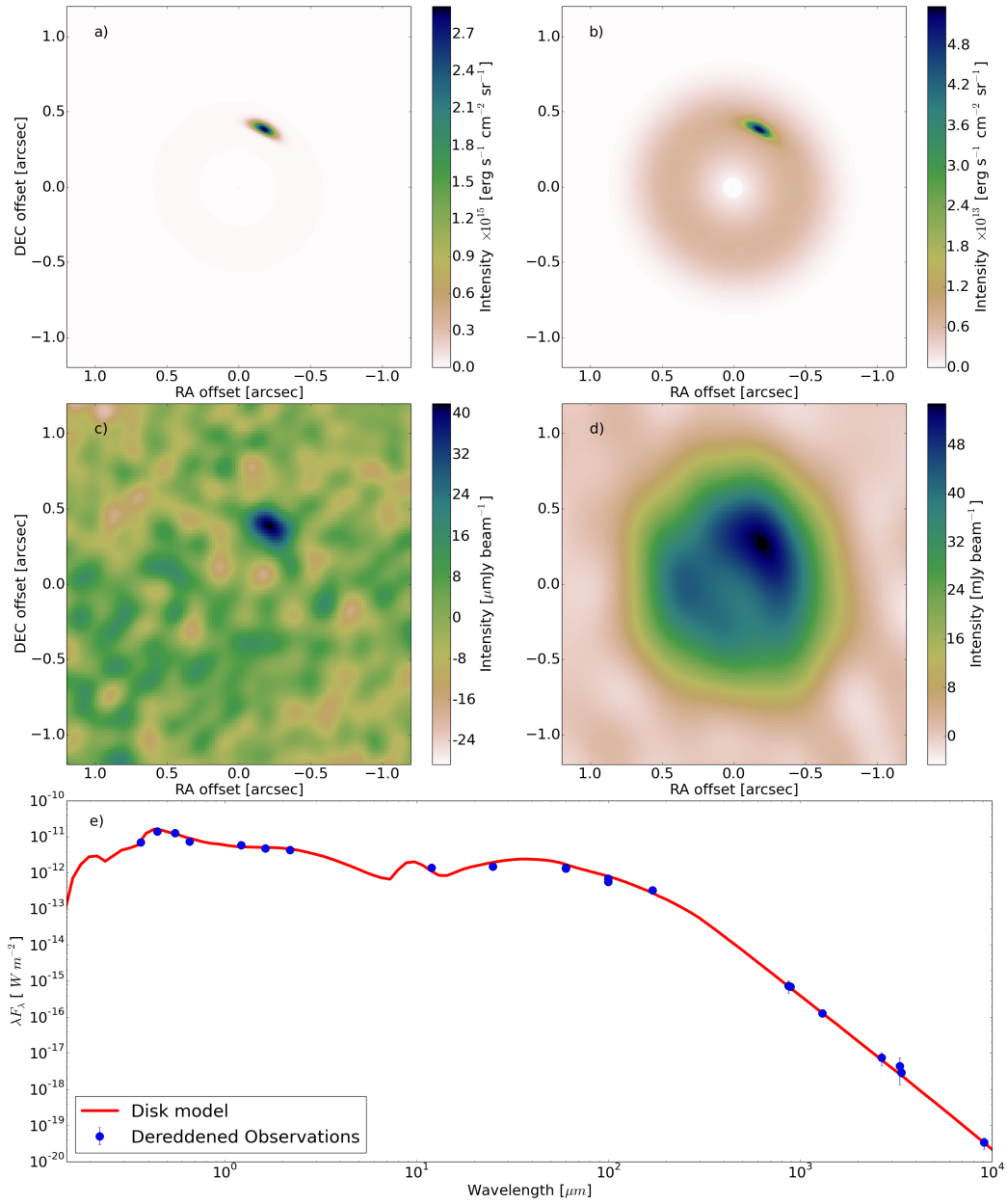

Figure 2.5: Parametric model predictions. (a) 33 GHz model image. (b) 337 GHz model image. (c) Simulated VLA Ka observation using the model image. (d) Simulated ALMA band 7 observation using the model image. (e) Dereddened SED of MWC 758 (blue dots) compared with the model (red line). Photometric data points were taken from [30, 37, 45, 64, 69] and the new VLA Ka and archival ALMA band 7 data presented in this work. We deredden the observations assuming a visual extinction A_V=0.22 [134] and an total-to-selective extinction ratio of R_V=3.1. The errorbars represent 2σ errors. In (a) and (b) the x & y axes indicate the offset in RA and DEC in arcsec, i.e. north is up and west is right.

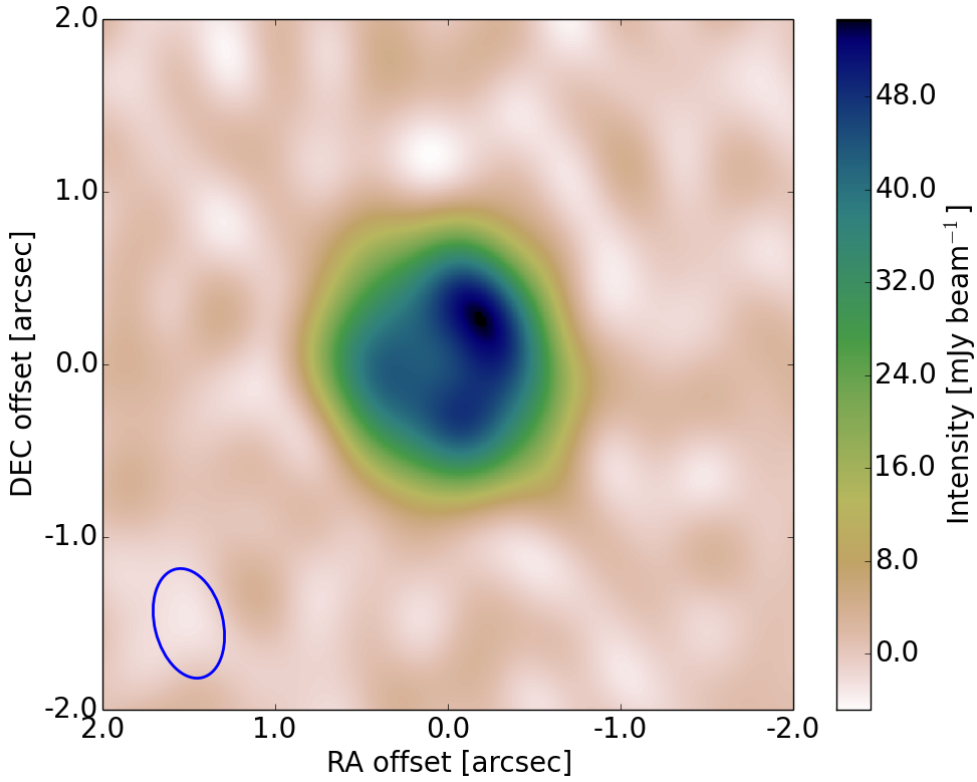

Figure 2.6: Simulated ALMA observation at 337 GHz using a parametric model with 2 vortices. The x & y axes indicate the offset in RA and DEC in arcsec, i.e. north is up and west is right.

2.3.5 Comparison with SPHERE PDI data

We also compare the VLA and ALMA observations with publicly available VLT SPHERE/IRDIS PDI (polarimetric differential imaging) data [11]. The data was taken on December 5, 2014 during the science verification time of SPHERE. MWC 758 was observed in DPI (dual polarimetric imaging) mode in Y-band (1.04 μm) with the IRDIS sub-instrument of SPHERE, with a 185 mas diameter coronagraphic mask and a Lyot apodizer. 70 exposures of 64 seconds each were taken, of which 48 (total integration time 51.2 minutes) were used for the reduction presented in this paper. PDI has proven to be a powerful technique to suppress the stellar light, and to first order approximates the reflected light off the disk surface by only measuring the polarized fraction of the light [7]. The frames were dark-subtracted, flat-fielded and bad pixels were removed, then centered. The polarized flux was calculated and instrumental effects accounted for in a way similar to that described in the Appendix of [7]. In Figure 2.7, the resulting SPHERE image reveals the disk outside of the inner working angle set by the coronagraph, including a strong, two-armed spiral.

Unlike the case of HD 142527, where a large cavity of ∼130 au is seen in scattered light [7] and in the sub-mm [24, 51], exposing the inner rim of the outer disk to stellar radiation, the SPHERE PDI Y-band image of MWC 758 shows that, down to the inner working angle (26 au), the cavity is not depleted of μm-sized dust grains traced at this wavelength. More-

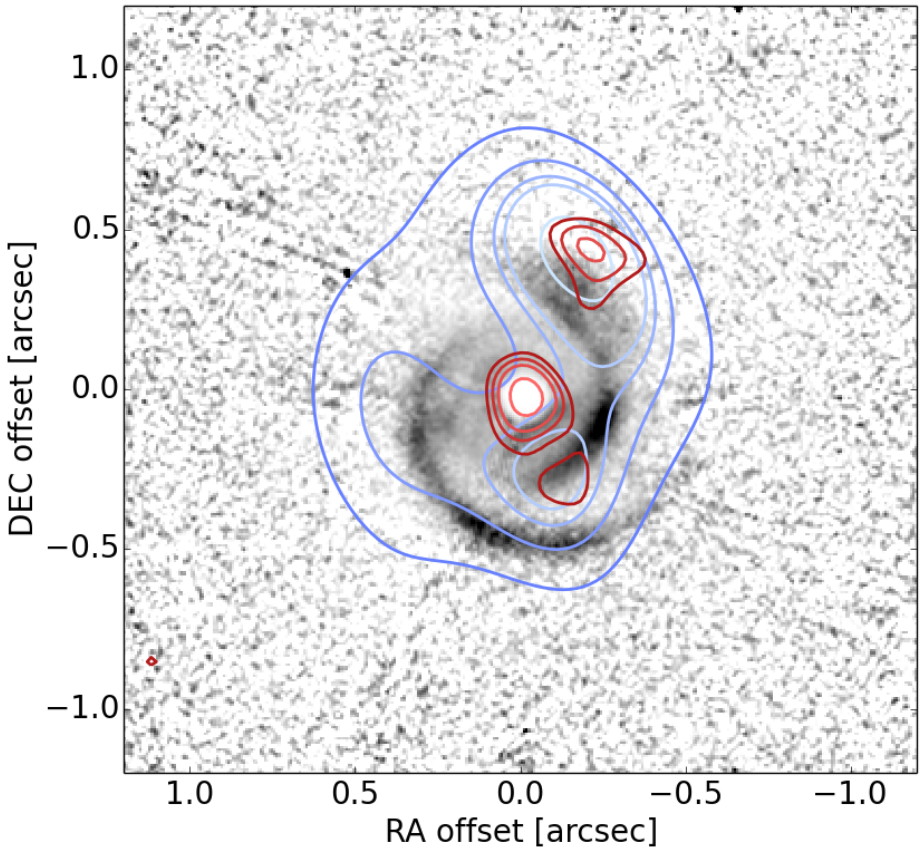

Figure 2.7: SPHERE-ALMA-VLA overlay. In grey scale, the polarised intensity scaled by r^2 to highlight the surface density of the disk. The decrement in the center correspond to the position of the coronagraph. The ALMA band 7 MEM map is represented in blue contours, while the restored VLA Ka map is presented in red contours. The contour levels are arbitrary to emphasise the disk morphology. The x & y axes indicate the offset in the RA and DEC in arcsec, i.e. north is up and west is right.

over, the polarized surface brightness drops abruptly behind the spiral arms, as if the arms shadowed the outer disk [55]. The presence of μm size dust grains could be linked to flaring of the gas disk, the mass of a possible gap-opening planet [48], or we might be looking at different stages of similar systems.

In the same figure, contours from the ALMA band 7 MEM and restored VLA Ka image are overplotted in blue and red, respectively. No evident correlation appears between the most southern spiral arm and the dust emission at 337 and 33 GHz, although we lack spatial resolution in the ALMA data to trace fine structures. On the other hand, the disk emission to the south of the star in the ALMA and VLA maps matches part of the western arm, while the VLA northern clump maximum is slightly offset ($\sim 0.2''$) from the SPHERE PDI maximum at the same PA. Such a radial displacement could be explained if there were a large wall of dust with a higher scale height shadowing the disk at the clump radius. This is probably related to a moderate or low flaring in the outer disk.

The SPHERE image also shows two decrements in the scattered light disk emission to

the north-east and south-west between two bright arms, with the former matching also a decrement in the ALMA MEM model that extends from the outer disk to the stellar position. The origin of these decrements could be related to a shadowing effect rather than a lack of material.

2.4 Discussion

MWC 758 shows spiral arms, non-axisymmetric dust thermal emission and asymmetries in the CO emission. The origin of all the disk asymmetries is hard to elucidate. A possible explanation for the non-axisymmetric disk seen at millimeter wavelength is a dust trap caused by a vortex. A steady state vortex as the one proposed in $L^2$13 cannot produce such a high contrast between the dust density in the vortex core and the disk background. A possible solution could be linked to the vortex tail which also causes dust trapping and can extend farther out from the vortex core [81, 82, 117]. Moreover, numerical MHD simulations have shown that high contrasts in the gas density field can be reached when large vortices form at the edge of planet induced gaps, surviving for $\sim$1000 orbits [146].

On the other hand, the azimuthal dust density structure in the outer disk is probably more complex than an azimuthal wavenumber m = 1. The second intensity maximum in the ALMA MEM model could be related to a second vortex at the inner edge of the outer disk. MHD simulations predict multiple vortices to form by the Rossby Wave Instability at the inner edges of "dead zones" [90]. Moreover, the decrement to the north-east in the ALMA and SPHERE images cannot be easily explained by a decrement in the dust density and a single vortex.

An alternative explanation to the asymmetry in the dust continuum emission at 337 GHz is that there is a strong asymmetry in the dust temperature field in the outer disk, similar to HD 142527 where a large crescent shows two peak intensities separated by a decrement in temperature caused by shadows cast by a tilted inner disk [26, 94]. If the decrements in MWC 758 are produced by a tilted or warped inner disk we would expect to see clear decrements almost opposite in azimuth, similar to the decrements in HD 142527 seen in polarized light [7]. Another possibility is that the spiral arms seen in scattered light [11, 55] cast shadows in the outer disk at different azimuth and radii. Moreover, a combination of both scenarios could be present. This could explain the asymmetric CO emission [69] as a temperature effect, the formation of spiral arms due to tidal forces from an inclined inner disk, or produced as a dynamic consequence of a perturbation of the gas temperature field [101]. However, the compact emission to the north-west of the star at centimeter wavelengths seen in the VLA maps suggests that the dust concentration is real, although azimuthal structure in the dust temperature field is expected as the disk is not axisymmetric.

The compact emission in the VLA Ka data could also be explained by a companion object, e.g. a forming planet accreting material. Such forming planet would have higher temperatures than a passive disk as it is accreting, also heating the disk around it. ALMA multi-band continuum and gas line observations would be ideal to disentangle if the VLA and ALMA band 7 asymmetries are density or temperature effects and if the VLA clump

is accreting or not. Additional H-α high contrast imaging could reveal the presence of an accreting companion.

2.5 Conclusions

We report new VLA observations at 33 and 15 GHz observations of the disk around the star MWC 758. The disk emission at these wavelengths traces the distribution of centimeter-sized dust grains. We found a compact disk emission at the same location where previous SMA and CARMA observations found deviations from an axisymmetric model at shorter wavelengths [69]. This compact emission is at $0.5''$ ($\sim$ 150 au) from the central star.

The VLA data also shows a strong compact emission coming from the star position, characterised by a spectral index of $\sim$0.5. This is likely due to free-free emission from the central star associated with a stellar wind or stellar accretion.

We compare these data with ALMA archival data, producing ALMA band 7 continuum deconvolved and restored images with a finer resolution than previous SMA and CARMA observations. Both maps show non-axisymmetric disk emission, with a peak intensity at the same location as the VLA clump, but more extended. These multiwavelength observations fit in the context of dust trapping, as the bigger grains traced at lower frequencies are more concentrated around pressure maxima than the ALMA emission around the maximum. However, in the ALMA maps the disk is not as resolved as in the VLA data. New ALMA long-baseline observations are needed to resolve better the disk morphology at millimeter wavelengths and to confirm the dust trapping effect.

In addition, we compare these observations with a new reduction of archival VLT SPHERE PDI images. There is an offset of $\sim 0.2''$ between the VLA clump and the north-western spiral feature. The same arm matches a second intensity maximum in the dust continuum seen in the VLA and ALMA maps. More interestingly, the decrement to the north-east in the ALMA MEM model matches a decrement in the polarized intensity, suggesting a shadowing effect rather than lack of material.

We develop a parametric non-axisymmetric model for the disk, incorporating a steady state vortex solution based on L^{2}13. Such a vortex cannot explain the decrement seen to the north-east of the star and a second maximum seen in the VLA and ALMA data. To reproduce the peak intensity of the ALMA image, we required to extend the vortex solution artificially beyond the shock perimeter. We also find that a second vortex could explain the extension to the south of the ALMA peak intensity and the decrement to the north-east.

MWC 758 is a very complex protoplanetary disk and there is still details to be addressed: what is the link between the possible vortex or vortices, and the spiral arms and apparent decrements? The missing piece of the puzzle might be found with a detailed study of the disk kinematics.

Conclusions

In this work we have studied two protoplanetary disks with clear signs of non-axial symmetry. These disks exhibit warps or azimuthal concentrations of big dust grains. These case studies are justified to understand the role of non-axial symmetry in disk astrophysics.

In the case of HD 142527, we studied the origin of two decrements seen in several previous observations in scattered light. Thanks to state-of-the-art radiative transfer tools, we studied the 3 dimensional structure of the system. We found a tilted or warped inner disk casting shadows on the outer disk, convincingly explaining the decrements. The inner disk must be inclined by 70±5 deg, and its PA is -8 ± 5 deg with respect to the outer disk.

We also compared our model predictions in the sub-mm with new ALMA observations, finding that the double-peaked structure of the large crescent is well reproduced by our model images. The shadowed regions can be interpreted as regions of lower temperature, and thus the thermal emission emerging from these regions will be slightly lower than its surroundings.

This warped disk raises theoretical questions on its origin: what kind of event or physical mechanism could be responsible for this extreme configuration? This finding opens the possibility to interpret scattered light images of disks from the perspective of warped structure casting non-axisymmetric shadows.

In Chapter 2 we analyzed new VLA observations at 33 and 15 GHz of the protoplanetary disk around the star MWC 758. Centimeter-sized grains, traced at these wavelengths, are highly concentrated in radius and azimuth in a compact region much smaller than the disk and unresolved by the VLA in B 0 configuration. This clump is located where previous observations found a deviation from axisymmetry at millimeter wavelengths, at $0.5''$ (~ 150 au) from the central star. We also detected emission at the stellar position, with a spectral index of $\sim$0.5. This is probably free-free emission due to stellar winds or stellar accretion.

To put the VLA data of MWC 758 into context, we compared with archival observations at different wavelengths. From archival ALMA data, we produced deconvolved and restored images at 337 GHz that show a non-axisymmetric disk with a peak intensity that coincides with the location of the VLA clump. The ALMA emission is more extended, this difference fits in the context of dust trapping in gas pressure maximum: big grains traded at longer wavelengths are more concentrated at the pressure maximum than smaller grains. This result holds even when degrading the resolution of the VLA data to match that of the ALMA data. New ALMA observations at millimetre wavelengths could measure the true extent of the dust grain segregation. Higher resolution ALMA data would also allow more stringent constraints

on the efficiency of trapping.

A new reduction of SPHERE PDI data was also done to compare with the VLA and ALMA images. We found almost no correlation between the scattered light and thermal emission. The SPHERE image is dominated by two bright spiral arms. There is an offset of $\sim 0.2''$ between the VLA clump and the north-western spiral feature. The same arm matches a second intensity maximum in the dust continuum seen in the VLA and ALMA maps. The SPHERE image also reveals a suspicious decrement also seen in the ALMA data suggesting a shadowing effect similar to HD 142527.

We develop a parametric non-axisymmetric model for the disk, incorporating a steady state vortex solution. We discovered that such a vortex cannot explain the decrement in polarized intensity and a second intensity maximum seen in the VLA and ALMA data. We also found that a second pressure maximum could explain the extension to the south of the ALMA peak intensity and the decrement to the north-east. However, the second-pressure maximum model is fine tuned, and this phase is predicted to be short lived and hence unlikely to be observed.

MWC 758 is a very complex protoplanetary disk and there are still important features to be addressed: what is the link between the possible dust trap and the spiral arms and apparent decrements? The missing piece of the puzzle might be found with a detailed study of the disk kinematics.

Finally, it has been demonstrated that in these two cases of transition disk, the disk structures are far from being axisymmetric. This could be general for other transitional disks, challenging our standard picture of axisymmetric disks.

Bibliography

[1] R. D. Alexander, C. J. Clarke, and J. E. Pringle. Photoevaporation of protoplanetary discs - I. Hydrodynamic models. *Monthly Notices of the Royal Astronomical Society*, 369(1):216–228, June 2006. ISSN 0035-8711. doi: 10.1111/j.1365-2966.2006.10293.x. URL `http://doi.wiley.com/10.1111/j.1365-2966.2006.10293.x`.

[2] R. D. Alexander, C. J. Clarke, and J. E. Pringle. Photoevaporation of protoplanetary discs - II. Evolutionary models and observable properties. *Monthly Notices of the Royal Astronomical Society*, 369(1):229–239, June 2006. ISSN 0035-8711. doi: 10.1111/j.1365-2966.2006.10294.x. URL `http://doi.wiley.com/10.1111/j.1365-2966.2006.10294.x`.

[3] P. Andre, D. Ward-Thompson, and M. Barsony. Submillimeter continuum observations of Rho Ophiuchi A - The candidate protostar VLA 1623 and prestellar clumps. ApJ, 406:122–141, March 1993. doi: 10.1086/172425.

[4] S. M. Andrews, D. J. Wilner, C. Espaillat, A. M. Hughes, C. P. Dullemond, M. K. McClure, C. Qi, and J. M. Brown. Resolved Images of Large Cavities in Protoplanetary Transition Disks. ApJ, 732:42, May 2011. doi: 10.1088/0004-637X/732/1/42.

[5] P. J. Armitage. *Astrophysics of Planet Formation*. ISBN 978-0-521-88745-8. Cambridge University Press., 2010.

[6] P. J. Armitage. Dynamics of Protoplanetary Disks. ARA&A, 49:195–236, September 2011. doi: 10.1146/annurev-astro-081710-102521.

[7] H. Avenhaus, S. P. Quanz, H. M. Schmid, M. R. Meyer, A. Garufi, S. Wolf, and C. Dominik. Structures in the Protoplanetary Disk of HD142527 Seen in Polarized Scattered Light. ApJ, 781:87, February 2014. doi: 10.1088/0004-637X/781/2/87.

[8] P. Barge and J. Sommeria. Did planet formation begin inside persistent gaseous vortices? A&A, 295:L1–L4, March 1995.

[9] N. M. Batalha, J. F. Rowe, S. T. Bryson, T. Barclay, C. J. Burke, D. A. Caldwell, J. L. Christiansen, F. Mullally, S. E. Thompson, T. M. Brown, A. K. Dupree, D. C. Fabrycky, E. B. Ford, J. J. Fortney, R. L. Gilliland, H. Isaacson, D. W. Latham, G. W. Marcy, S. N. Quinn, D. Ragozzine, A. Shporer, W. J. Borucki, D. R. Ciardi, T. N. Gautier, III, M. R. Haas, J. M. Jenkins, D. G. Koch, J. J. Lissauer, W. Rapin, G. S. Basri, A. P. Boss, L. A. Buchhave, J. A. Carter, D. Charbonneau, J. Christensen-Dalsgaard, B. D. Clarke,

W. D. Cochran, B.-O. Demory, J.-M. Desert, E. Devore, L. R. Doyle, G. A. Esquerdo, M. Everett, F. Fressin, J. C. Geary, F. R. Girouard, A. Gould, J. R. Hall, M. J. Holman, A. W. Howard, S. B. Howell, K. A. Ibrahim, K. Kinemuchi, H. Kjeldsen, T. C. Klaus, J. Li, P. W. Lucas, S. Meibom, R. L. Morris, A. Prša, E. Quintana, D. T. Sanderfer, D. Sasselov, S. E. Seader, J. C. Smith, J. H. Steffen, M. Still, M. C. Stumpe, J. C. Tarter, P. Tenenbaum, G. Torres, J. D. Twicken, K. Uddin, J. Van Cleve, L. Walkowicz, and W. F. Welsh. Planetary Candidates Observed by Kepler. III. Analysis of the First 16 Months of Data. ApJS, 204:24, February 2013. doi: 10.1088/0067-0049/204/2/24.

[10] S. V. W. Beckwith, A. I. Sargent, R. S. Chini, and R. Guesten. A survey for circumstellar disks around young stellar objects. AJ, 99:924–945, March 1990. doi: 10.1086/115385.

[11] M. Benisty, A. Juhasz, A. Boccaletti, H. Avenhaus, J. Milli, C. Thalmann, C. Dominik, P. Pinilla, E. Buenzli, A. Pohl, J.-L. Beuzit, T. Birnstiel, J. de Boer, M. Bonnefoy, G. Chauvin, V. Christiaens, A. Garufi, C. Grady, T. Henning, N. Huelamo, A. Isella, M. Langlois, F. Menard, D. Mouillet, J. Olofsson, E. Pantin, C. Pinte, and L. Pueyo. Asymmetric features in the protoplanetary disk MWC758. *ArXiv e-prints*, May 2015.

[12] N. G. Beskrovnaya, M. A. Pogodin, A. S. Miroshnichenko, P. S. Thé, I. S. Savanov, N. M. Shakhovskoy, A. N. Rostopchina, O. V. Kozlova, and K. S. Kuratov. Spectroscopic, photometric, and polarimetric study of the Herbig AE candidate HD 36112. A&A, 343:163–174, March 1999.

[13] B. Biller, S. Lacour, A. Juhász, M. Benisty, G. Chauvin, J. Olofsson, J.-U. Pott, A. Müller, A. Sicilia-Aguilar, M. Bonnefoy, P. Tuthill, P. Thebault, T. Henning, and A. Crida. A Likely Close-in Low-mass Stellar Companion to the Transitional Disk Star HD 142527. ApJ, 753:L38, July 2012. doi: 10.1088/2041-8205/753/2/L38.

[14] J. Binney. WARPS. ARA&A, 30:51–74, 1992. doi: 10.1146/annurev.aa.30.090192.000411.

[15] T. Birnstiel, C. P. Dullemond, and P. Pinilla. Lopsided dust rings in transition disks. A&A, 550:L8, February 2013. doi: 10.1051/0004-6361/201220847.

[16] Craig F. Bohren and D.R. Huffman. *Absorption and scattering of light by small particles*. Wiley science paperback series. Wiley, 1983. ISBN 9780471293408. URL `http://books.google.cl/books?id=S1RCZ8BjgN0C`.

[17] A. C. Boley. The Two Modes of Gas Giant Planet Formation. ApJ, 695:L53–L57, April 2009. doi: 10.1088/0004-637X/695/1/L53.

[18] W. J. Borucki, D. G. Koch, G. Basri, N. Batalha, A. Boss, T. M. Brown, D. Caldwell, J. Christensen-Dalsgaard, W. D. Cochran, E. DeVore, E. W. Dunham, A. K. Dupree, T. N. Gautier, III, J. C. Geary, R. Gilliland, A. Gould, S. B. Howell, J. M. Jenkins, H. Kjeldsen, D. W. Latham, J. J. Lissauer, G. W. Marcy, D. G. Monet, D. Sasselov, J. Tarter, D. Charbonneau, L. Doyle, E. B. Ford, J. Fortney, M. J. Holman, S. Seager, J. H. Steffen, W. F. Welsh, C. Allen, S. T. Bryson, L. Buchhave, H. Chandrasekaran,

J. L. Christiansen, D. Ciardi, B. D. Clarke, J. L. Dotson, M. Endl, D. Fischer, F. Fressin, M. Haas, E. Horch, A. Howard, H. Isaacson, J. Kolodziejczak, J. Li, P. MacQueen, S. Meibom, A. Prsa, E. V. Quintana, J. Rowe, W. Sherry, P. Tenenbaum, G. Torres, J. D. Twicken, J. Van Cleve, L. Walkowicz, and H. Wu. Characteristics of Kepler Planetary Candidates Based on the First Data Set. ApJ, 728:117, February 2011. doi: 10.1088/0004-637X/728/2/117.

[19] A. P. Boss. Giant planet formation by gravitational instability. *Science*, 276:1836–1839, 1997. doi: 10.1126/science.276.5320.1836.

[20] F. Brauer, C. P. Dullemond, and T. Henning. Coagulation, fragmentation and radial motion of solid particles in protoplanetary disks. A&A, 480:859–877, March 2008. doi: 10.1051/0004-6361:20077759.

[21] H. Canovas, F. Ménard, A. Hales, A. Jordán, M. R. Schreiber, S. Casassus, T. M. Gledhill, and C. Pinte. Near-infrared imaging polarimetry of HD 142527. A&A, 556: A123, August 2013. doi: 10.1051/0004-6361/201321924.

[22] S. Casassus, S. Perez M., A. Jordán, F. Ménard, J. Cuadra, M. R. Schreiber, A. S. Hales, and B. Ercolano. The Dynamically Disrupted Gap in HD 142527. ApJ, 754: L31, August 2012. doi: 10.1088/2041-8205/754/2/L31.

[23] S. Casassus, S. M. Perez, G. van der Plas, W. R. F. Dent, A. Hales, and F. Ménard. ALMA results on a case-study transition disk. *NRAO workshop: Transformational Science with ALMA: From Dust to Rocks to Planets*, April 2013.

[24] S. Casassus, G. van der Plas, S. Perez, and et al. Flows of gas through a protoplanetary gap. *Nature*, January 2013.

[25] S. Casassus, G. van der Plas, S. M. Perez, W. R. F. Dent, E. Fomalont, J. Hagelberg, A. Hales, A. Jordán, D. Mawet, F. Ménard, A. Wootten, D. Wilner, A. M. Hughes, M. R. Schreiber, J. H. Girard, B. Ercolano, H. Canovas, P. E. Román, and V. Salinas. Flows of gas through a protoplanetary gap. Nature, 493:191–194, January 2013. doi: 10.1038/nature11769.

[26] S. Casassus, C. Wright, S. Marino, S. Maddison, A. Wootten, P. Roman, S. Pérez, P. Pinilla, M. Wyatt, V. Moral, F. Ménard, V. Christiaens, L. Cieza, and G. van der Plas. A compact concentration of large grains in a protoplanetary dust trap. *submitted to ApJ*, May 2015.

[27] S. et al. Casassus. . in prep, 2015.

[28] A. Cassan, D. Kubas, J.-P. Beaulieu, M. Dominik, K. Horne, J. Greenhill, J. Wambsganss, J. Menzies, A. Williams, U. G. Jørgensen, A. Udalski, D. P. Bennett, M. D. Albrow, V. Batista, S. Brillant, J. A. R. Caldwell, A. Cole, C. Coutures, K. H. Cook, S. Dieters, D. D. Prester, J. Donatowicz, P. Fouqué, K. Hill, N. Kains, S. Kane, J.-B. Marquette, R. Martin, K. R. Pollard, K. C. Sahu, C. Vinter, D. Warren, B. Watson, M. Zub, T. Sumi, M. K. Szymański, M. Kubiak, R. Poleski, I. Soszynski, K. Ulaczyk, G. Pietrzyński, and Ł. Wyrzykowski. One or more bound planets per

Milky Way star from microlensing observations. Nature, 481:167–169, January 2012. doi: 10.1038/nature10684.

[29] F. Castelli and R. L. Kurucz. New Grids of ATLAS9 Model Atmospheres. In N. Piskunov, W. W. Weiss, & D. F. Gray, editor, *Modelling of Stellar Atmospheres*, volume 210 of *IAU Symposium*, pages 20P–+, 2003.

[30] E. Chapillon, S. Guilloteau, A. Dutrey, and V. Piétu. Disks around CQ Tauri and MWC 758: dense PDR or gas dispersal? A&A, 488:565–578, September 2008. doi: 10.1051/0004-6361:200809523.

[31] E. et al. Chapillon. . in prep, 2015.

[32] G. Chauvin, A.-M. Lagrange, H. Beust, M. Bonnefoy, A. Boccaletti, D. Apai, F. Allard, D. Ehrenreich, J. H. V. Girard, D. Mouillet, and D. Rouan. Orbital characterization of the β Pictoris b giant planet. A&A, 542:A41, June 2012. doi: 10.1051/0004-6361/201118346.

[33] V. Christiaens, S. Casassus, S. Perez, G. van der Plas, and F. Ménard. . *submitted to* ApJ, 2014.

[34] L. Cieza, D. L. Padgett, K. R. Stapelfeldt, J.-C. Augereau, P. Harvey, N. J. Evans, II, B. Merín, D. Koerner, A. Sargent, E. F. van Dishoeck, L. Allen, G. Blake, T. Brooke, N. Chapman, T. Huard, S.-P. Lai, L. Mundy, P. C. Myers, W. Spiesman, and Z. Wahhaj. The Spitzer c2d Survey of Weak-Line T Tauri Stars. II. New Constraints on the Timescale for Planet Building. ApJ, 667:308–328, September 2007. doi: 10.1086/520698.

[35] C. J. Clarke, A. Gendrin, and M. Sotomayor. The dispersal of circumstellar discs: the role of the ultraviolet switch. MNRAS, 328:485–491, December 2001. doi: 10.1046/j.1365-8711.2001.04891.x.

[36] L. M. Close, K. B. Follette, J. R. Males, A. Puglisi, M. Xompero, D. Apai, J. Najita, A. J. Weinberger, K. Morzinski, T. J. Rodigas, P. Hinz, V. Bailey, and R. Briguglio. Discovery of Hα Emission from the Close Companion inside the Gap of Transitional Disk HD 142527. ApJ, 781:L30, February 2014. doi: 10.1088/2041-8205/781/2/L30.

[37] R. M. Cutri, M. F. Skrutskie, S. van Dyk, C. A. Beichman, J. M. Carpenter, T. Chester, L. Cambresy, T. Evans, J. Fowler, J. Gizis, E. Howard, J. Huchra, T. Jarrett, E. L. Kopan, J. D. Kirkpatrick, R. M. Light, K. A. Marsh, H. McCallon, S. Schneider, R. Stiening, M. Sykes, M. Weinberg, W. A. Wheaton, S. Wheelock, and N. Zacarias. VizieR Online Data Catalog: 2MASS All-Sky Catalog of Point Sources (Cutri+ 2003). *VizieR Online Data Catalog*, 2246:0, June 2003.

[38] R. I. Dawson, R. A. Murray-Clay, and D. C. Fabrycky. On the Misalignment of the Directly Imaged Planet β Pictoris b with the System's Warped Inner Disk. ApJ, 743:L17, December 2011. doi: 10.1088/2041-8205/743/1/L17.

[39] R. Descartes. *Principia philosophiae*. apud Ludovicum Elzevirium, 1644. URL `http:`

//books.google.cl/books?id=lHpbAAAAQAAJ.

[40] B. T. Draine. Scattering by Interstellar Dust Grains. I. Optical and Ultraviolet. ApJ, 598:1017–1025, December 2003. doi: 10.1086/379118.

[41] B. Dubrulle, L. Marié, C. Normand, D. Richard, F. Hersant, and J.-P. Zahn. An hydrodynamic shear instability in stratified disks. A&A, 429:1–13, January 2005. doi: 10.1051/0004-6361:200400065.

[42] C. P. Dullemond and J. D. Monnier. The Inner Regions of Protoplanetary Disks. ARA&A, 48:205–239, September 2010. doi: 10.1146/annurev-astro-081309-130932.

[43] C.P. Dullemond, A. Juhasz, A. Pohl, F. Sereshti, R. Shetty, T. Peters, B. Commercon, and M. Flock. Radmc3d v0.38 http://www.ita.uni-heidelberg.de/dullemond/software/radmc-3d/, 2014.

[44] C.P. Dullemond, A. Juhasz, A. Pohl, F. Sereshti, R. Shetty, T. Peters, B. Commercon, and M. Flock. Radmc3d v0.39 http://www.ita.uni-heidelberg.de/dullemond/software/radmc-3d/, 2015.

[45] D. Elia, F. Strafella, L. Campeggio, B. Maiolo, and S. Pezzuto. An ISO-LWS two-colour diagram of Herbig Ae/Be stars. *New Astronomy*, 10:545–550, July 2005. doi: 10.1016/j.newast.2005.03.006.

[46] C. Espaillat, J. Muzerolle, J. Najita, S. Andrews, Z. Zhu, N. Calvet, S. Kraus, J. Hashimoto, A. Kraus, and P. D'Alessio. An Observational Perspective of Transitional Disks. *Protostars and Planets VI*, pages 497–520, 2014. doi: 10.2458/azu_uapress_9780816531240-ch022.

[47] N. J. Evans, II, M. M. Dunham, J. K. Jørgensen, M. L. Enoch, B. Merín, E. F. van Dishoeck, J. M. Alcalá, P. C. Myers, K. R. Stapelfeldt, T. L. Huard, L. E. Allen, P. M. Harvey, T. van Kempen, G. A. Blake, D. W. Koerner, L. G. Mundy, D. L. Padgett, and A. I. Sargent. The Spitzer c2d Legacy Results: Star-Formation Rates and Efficiencies; Evolution and Lifetimes. ApJS, 181:321, April 2009. doi: 10.1088/0067-0049/181/2/321.

[48] L. Fouchet, J.-F. Gonzalez, and S. T. Maddison. Planet gaps in the dust layer of 3D protoplanetary disks. I. Hydrodynamical simulations of T Tauri disks. A&A, 518:A16, July 2010. doi: 10.1051/0004-6361/200913778.

[49] H. Fujiwara, M. Honda, H. Kataza, T. Yamashita, T. Onaka, M. Fukagawa, Y. K. Okamoto, T. Miyata, S. Sako, T. Fujiyoshi, and I. Sakon. The Asymmetric Thermal Emission of the Protoplanetary Disk Surrounding HD 142527 Seen by Subaru/COMICS. ApJ, 644:L133–L136, June 2006. doi: 10.1086/505597.

[50] M. Fukagawa, M. Tamura, Y. Itoh, T. Kudo, Y. Imaeda, Y. Oasa, S. S. Hayashi, and M. Hayashi. Near-Infrared Images of Protoplanetary Disk Surrounding HD 142527. ApJ, 636:L153–L156, January 2006. doi: 10.1086/500128.

[51] M. Fukagawa, T. Tsukagoshi, M. Momose, K. Saigo, N. Ohashi, Y. Kitamura, S.-i. Inutsuka, T. Muto, H. Nomura, T. Takeuchi, H. Kobayashi, T. Hanawa, E. Akiyama, M. Honda, H. Fujiwara, A. Kataoka, S. Z. Takahashi, and H. Shibai. Local Enhancement of the Surface Density in the Protoplanetary Ring Surrounding HD 142527. PASJ, 65:L14, December 2013. doi: 10.1093/pasj/65.6.L14.

[52] G. Gamow and J. A. Hynek. A New Theory by C. F. Von WEIZSÄCKER of the Origin of the Planetary Systen. ApJ, 101:249–254, March 1945. doi: 10.1086/144711.

[53] R. Garcia Lopez, A. Natta, L. Testi, and E. Habart. Accretion rates in Herbig Ae stars. A&A, 459:837–842, December 2006. doi: 10.1051/0004-6361:20065575.

[54] J. Goodman, R. Narayan, and P. Goldreich. The stability of accretion tori. II - Nonlinear evolution to discrete planets. MNRAS, 225:695–711, April 1987.

[55] C. A. Grady, T. Muto, J. Hashimoto, M. Fukagawa, T. Currie, B. Biller, C. Thalmann, M. L. Sitko, R. Russell, J. Wisniewski, R. Dong, J. Kwon, S. Sai, J. Hornbeck, G. Schneider, D. Hines, A. Moro Martín, M. Feldt, T. Henning, J.-U. Pott, M. Bonnefoy, J. Bouwman, S. Lacour, A. Mueller, A. Juhász, A. Crida, G. Chauvin, S. Andrews, D. Wilner, A. Kraus, S. Dahm, T. Robitaille, H. Jang-Condell, L. Abe, E. Akiyama, W. Brandner, T. Brandt, J. Carson, S. Egner, K. B. Follette, M. Goto, O. Guyon, Y. Hayano, M. Hayashi, S. Hayashi, K. Hodapp, M. Ishii, M. Iye, M. Janson, R. Kandori, G. Knapp, T. Kudo, N. Kusakabe, M. Kuzuhara, S. Mayama, M. McElwain, T. Matsuo, S. Miyama, J.-I. Morino, T. Nishimura, T.-S. Pyo, G. Serabyn, H. Suto, R. Suzuki, M. Takami, N. Takato, H. Terada, D. Tomono, E. Turner, M. Watanabe, T. Yamada, H. Takami, T. Usuda, and M. Tamura. Spiral Arms in the Asymmetrically Illuminated Disk of MWC 758 and Constraints on Giant Planets. ApJ, 762:48, January 2013. doi: 10.1088/0004-637X/762/1/48.

[56] R. A. Gutermuth, P. C. Myers, S. T. Megeath, L. E. Allen, J. L. Pipher, J. Muzerolle, A. Porras, E. Winston, and G. Fazio. Spitzer Observations of NGC 1333: A Study of Structure and Evolution in a Nearby Embedded Cluster. ApJ, 674:336–356, February 2008. doi: 10.1086/524722.

[57] C. Güttler, J. Blum, A. Zsom, C. W. Ormel, and C. P. Dullemond. The outcome of protoplanetary dust growth: pebbles, boulders, or planetesimals?. I. Mapping the zoo of laboratory collision experiments. A&A, 513:A56, April 2010. doi: 10.1051/0004-6361/200912852.

[58] N. Haghighipour and A. P. Boss. On Pressure Gradients and Rapid Migration of Solids in a Nonuniform Solar Nebula. ApJ, 583:996–1003, February 2003. doi: 10.1086/345472.

[59] P. Hartigan, S. Edwards, and L. Ghandour. Disk Accretion and Mass Loss from Young Stars. ApJ, 452:736, October 1995. doi: 10.1086/176344.

[60] L. Hartmann, N. Calvet, E. Gullbring, and P. D'Alessio. Accretion and the Evolution of T Tauri Disks. ApJ, 495:385–400, March 1998. doi: 10.1086/305277.

[61] T. Henning and H. Mutschke. Low-temperature infrared properties of cosmic dust analogues. A&A, 327:743–754, November 1997.

[62] L. G. Henyey and J. L. Greenstein. Diffuse radiation in the Galaxy. ApJ, 93:70–83, January 1941. doi: 10.1086/144246.

[63] J. Hernández, L. Hartmann, T. Megeath, R. Gutermuth, J. Muzerolle, N. Calvet, A. K. Vivas, C. Briceño, L. Allen, J. Stauffer, E. Young, and G. Fazio. A Spitzer Space Telescope Study of Disks in the Young σ Orionis Cluster. ApJ, 662:1067–1081, June 2007. doi: 10.1086/513735.

[64] E. Hög, C. Fabricius, V. V. Makarov, S. Urban, T. Corbin, G. Wycoff, U. Bastian, P. Schwekendiek, and A. Wicenec. The Tycho-2 catalogue of the 2.5 million brightest stars. A&A, 355:L27–L30, March 2000.

[65] D. Hollenbach, D. Johnstone, S. Lizano, and F. Shu. Photoevaporation of disks around massive stars and application to ultracompact H II regions. ApJ, 428:654–669, June 1994. doi: 10.1086/174276.

[66] C. Hunter and A. Toomre. Dynamics of the Bending of the Galaxy. ApJ, 155:747, March 1969. doi: 10.1086/149908.

[67] S. Inaba and P. Barge. Dusty Vortices in Protoplanetary Disks. ApJ, 649:415–427, September 2006. doi: 10.1086/506427.

[68] A. Isella, E. Tatulli, A. Natta, and L. Testi. Gas and dust in the inner disk of the Herbig Ae star MWC 758. A&A, 483:L13–L16, May 2008. doi: 10.1051/0004-6361:200809641.

[69] A. Isella, A. Natta, D. Wilner, J. M. Carpenter, and L. Testi. Millimeter Imaging of MWC 758: Probing the Disk Structure and Kinematics. ApJ, 725:1735–1741, December 2010. doi: 10.1088/0004-637X/725/2/1735.

[70] A. Isella, L. M. Pérez, J. M. Carpenter, L. Ricci, S. Andrews, and K. Rosenfeld. An Azimuthal Asymmetry in the LkHα 330 Disk. ApJ, 775:30, September 2013. doi: 10.1088/0004-637X/775/1/30.

[71] A. Johansen, A. C. Andersen, and A. Brandenburg. Simulations of dust-trapping vortices in protoplanetary discs. A&A, 417:361–374, April 2004. doi: 10.1051/0004-6361:20034417.

[72] P. Kalas, J. R. Graham, E. Chiang, M. P. Fitzgerald, M. Clampin, E. S. Kite, K. Stapelfeldt, C. Marois, and J. Krist. Optical Images of an Exosolar Planet 25 Light-Years from Earth. *Science*, 322:1345–, November 2008. doi: 10.1126/science.1166609.

[73] I. Kant. *Allgemeine Naturgeschichte und Theorie des Himmels*. 1755.

[74] H. H. Klahr and T. Henning. Particle-Trapping Eddies in Protoplanetary Accretion Disks. *Icarus*, 128:213–229, July 1997. doi: 10.1006/icar.1997.5720.

[75] S. Kothe, C. Güttler, and J. Blum. The Physics of Protoplanetesimal Dust Agglomerates. V. Multiple Impacts of Dusty Agglomerates at Velocities Above the Fragmentation Threshold. ApJ, 725:1242–1251, December 2010. doi: 10.1088/0004-637X/725/1/1242.

[76] M. Kuzuhara, M. Tamura, T. Kudo, M. Janson, R. Kandori, T. D. Brandt, C. Thalmann, D. Spiegel, B. Biller, J. Carson, Y. Hori, R. Suzuki, A. Burrows, T. Henning, E. L. Turner, M. W. McElwain, A. Moro-Martín, T. Suenaga, Y. H. Takahashi, J. Kwon, P. Lucas, L. Abe, W. Brandner, S. Egner, M. Feldt, H. Fujiwara, M. Goto, C. A. Grady, O. Guyon, J. Hashimoto, Y. Hayano, M. Hayashi, S. S. Hayashi, K. W. Hodapp, M. Ishii, M. Iye, G. R. Knapp, T. Matsuo, S. Mayama, S. Miyama, J.-I. Morino, J. Nishikawa, T. Nishimura, T. Kotani, N. Kusakabe, T.-S. Pyo, E. Serabyn, H. Suto, M. Takami, N. Takato, H. Terada, D. Tomono, M. Watanabe, J. P. Wisniewski, T. Yamada, H. Takami, and T. Usuda. Direct Imaging of a Cold Jovian Exoplanet in Orbit around the Sun-like Star GJ 504. ApJ, 774:11, September 2013. doi: 10.1088/0004-637X/774/1/11.

[77] C. J. Lada and B. A. Wilking. The nature of the embedded population in the Rho Ophiuchi dark cloud - Mid-infrared observations. ApJ, 287:610–621, December 1984. doi: 10.1086/162719.

[78] C. J. Lada, A. A. Muench, K. L. Luhman, L. Allen, L. Hartmann, T. Megeath, P. Myers, G. Fazio, K. Wood, J. Muzerolle, G. Rieke, N. Siegler, and E. Young. Spitzer Observations of IC 348: The Disk Population at 2-3 Million Years. AJ, 131:1574–1607, March 2006. doi: 10.1086/499808.

[79] A.-M. Lagrange, D. Gratadour, G. Chauvin, T. Fusco, D. Ehrenreich, D. Mouillet, G. Rousset, D. Rouan, F. Allard, É. Gendron, J. Charton, L. Mugnier, P. Rabou, J. Montri, and F. Lacombe. A probable giant planet imaged in the β Pictoris disk. VLT/NaCo deep L'-band imaging. A&A, 493:L21–L25, January 2009. doi: 10.1051/0004-6361:200811325.

[80] A.-M. Lagrange, A. Boccaletti, J. Milli, G. Chauvin, M. Bonnefoy, D. Mouillet, J. C. Augereau, J. H. Girard, S. Lacour, and D. Apai. The position of β Pictoris b position relative to the debris disk. A&A, 542:A40, June 2012. doi: 10.1051/0004-6361/201118274.

[81] G. Lesur and J. C. B. Papaloizou. On the stability of elliptical vortices in accretion discs. A&A, 498:1–12, April 2009. doi: 10.1051/0004-6361/200811577.

[82] G. Lesur and J. C. B. Papaloizou. The subcritical baroclinic instability in local accretion disc models. A&A, 513:A60, April 2010. doi: 10.1051/0004-6361/200913594.

[83] A. Li and J. M. Greenberg. A unified model of interstellar dust. A&A, 323:566–584, July 1997.

[84] D. N. C. Lin and J. Papaloizou. On the tidal interaction between protoplanets and the protoplanetary disk. III - Orbital migration of protoplanets. ApJ, 309:846–857, October 1986. doi: 10.1086/164653.

[85] S. H. Lubow and G. D'Angelo. Gas Flow across Gaps in Protoplanetary Disks. ApJ, 641:526–533, April 2006. doi: 10.1086/500356.

[86] S. H. Lubow, M. Seibert, and P. Artymowicz. Disk Accretion onto High-Mass Planets. ApJ, 526:1001–1012, December 1999. doi: 10.1086/308045.

[87] D. Lynden-Bell and A. J. Kalnajs. On the generating mechanism of spiral structure. MNRAS, 157:1, 1972.

[88] D. Lynden-Bell and J. E. Pringle. The evolution of viscous discs and the origin of the nebular variables. MNRAS, 168:603–637, September 1974.

[89] W. Lyra and M.-K. Lin. Steady State Dust Distributions in Disk Vortices: Observational Predictions and Applications to Transitional Disks. ApJ, 775:17, September 2013. doi: 10.1088/0004-637X/775/1/17.

[90] W. Lyra and M.-M. Mac Low. Rossby Wave Instability at Dead Zone Boundaries in Three-dimensional Resistive Magnetohydrodynamical Global Models of Protoplanetary Disks. ApJ, 756:62, September 2012. doi: 10.1088/0004-637X/756/1/62.

[91] W. Lyra, A. Johansen, H. Klahr, and N. Piskunov. Embryos grown in the dead zone. Assembling the first protoplanetary cores in low mass self-gravitating circumstellar disks of gas and solids. A&A, 491:L41–L44, December 2008. doi: 10.1051/0004-6361:200810626.

[92] W. Lyra, A. Johansen, H. Klahr, and N. Piskunov. Standing on the shoulders of giants. Trojan Earths and vortex trapping in low mass self-gravitating protoplanetary disks of gas and solids. A&A, 493:1125–1139, January 2009. doi: 10.1051/0004-6361:200810797.

[93] E. E. Mamajek. Initial Conditions of Planet Formation: Lifetimes of Primordial Disks. In T. Usuda, M. Tamura, and M. Ishii, editors, *American Institute of Physics Conference Series*, volume 1158 of *American Institute of Physics Conference Series*, pages 3–10, August 2009. doi: 10.1063/1.3215910.

[94] S. Marino, S. Perez, and S. Casassus. Shadows Cast by a Warp in the HD 142527 Protoplanetary Disk. ApJ, 798:L44, January 2015. doi: 10.1088/2041-8205/798/2/L44.

[95] C. Marois, B. Macintosh, T. Barman, B. Zuckerman, I. Song, J. Patience, D. Lafrenière, and R. Doyon. Direct Imaging of Multiple Planets Orbiting the Star HR 8799. *Science*, 322:1348–, November 2008. doi: 10.1126/science.1166585.

[96] M. Mayor and D. Queloz. A Jupiter-mass companion to a solar-type star. Nature, 378: 355–359, November 1995. doi: 10.1038/378355a0.

[97] M. Mayor, M. Marmier, C. Lovis, S. Udry, D. Ségransan, F. Pepe, W. Benz, J. . Bertaux, F. Bouchy, X. Dumusque, G. Lo Curto, C. Mordasini, D. Queloz, and N. C. Santos. The HARPS search for southern extra-solar planets XXXIV. Occurrence, mass distribution and orbital properties of super-Earths and Neptune-mass planets. *ArXiv e-prints*, September 2011.

[98] G. Meeus, B. Montesinos, I. Mendigutía, I. Kamp, W. F. Thi, C. Eiroa, C. A. Grady, G. Mathews, G. Sandell, C. Martin-Zaïdi, S. Brittain, W. R. F. Dent, C. Howard, F. Ménard, C. Pinte, A. Roberge, B. Vandenbussche, and J. P. Williams. Observations of Herbig Ae/Be stars with Herschel/PACS. The atomic and molecular contents of their protoplanetary discs. A&A, 544:A78, August 2012. doi: 10.1051/0004-6361/201219225.

[99] H. Meheut, R. Keppens, F. Casse, and W. Benz. Formation and long-term evolution of 3D vortices in protoplanetary discs. A&A, 542:A9, June 2012. doi: 10.1051/0004-6361/201118500.

[100] H. Mizuno. Formation of the Giant Planets. *Progress of Theoretical Physics*, 64:544–557, August 1980. doi: 10.1143/PTP.64.544.

[101] M. et al. Montesinos. . in prep, 2015.

[102] D. Mouillet, J. D. Larwood, J. C. B. Papaloizou, and A. M. Lagrange. A planet on an inclined orbit as an explanation of the warp in the Beta Pictoris disc. MNRAS, 292: 896, December 1997.

[103] G. D. Mulders, S.-J. Paardekooper, O. Panić, C. Dominik, R. van Boekel, and T. Ratzka. Planet or brown dwarf? Inferring the companion mass in HD 100546 from the wall shape using mid-infrared interferometry. A&A, 557:A68, September 2013. doi: 10.1051/0004-6361/201220930.

[104] J. Muzerolle, N. Calvet, and L. Hartmann. Magnetospheric Accretion Models for the Hydrogen Emission Lines of T Tauri Stars. ApJ, 492:743–753, January 1998. doi: 10.1086/305069.

[105] N. Ohashi. Observational signature of planet formation: The ALMA view. Ap&SS, 313:101–107, January 2008. doi: 10.1007/s10509-007-9667-5.

[106] J. C. Papaloizou and G. J. Savonije. Instabilities in self-gravitating gaseous discs. MNRAS, 248:353–369, February 1991.

[107] L. M. Pérez, A. Isella, J. M. Carpenter, and C. J. Chandler. Large-scale Asymmetries in the Transitional Disks of SAO 206462 and SR 21. ApJ, 783:L13, March 2014. doi: 10.1088/2041-8205/783/1/L13.

[108] S. Perez, S. Casassus, F. Ménard, P. Roman, G. van der Plas, L. Cieza, C. Pinte, V. Christiaens, and A. S. Hales. CO Gas Inside the Protoplanetary Disk Cavity in HD 142527: Disk Structure from ALMA. ApJ, 798:85, January 2015. doi: 10.1088/0004-637X/798/2/85.

[109] F. Perri and A. G. W. Cameron. Hydrodynamic instability of the solar nebula in the presence of a planetary core. *Icarus*, 22:416–425, August 1974. doi: 10.1016/0019-1035(74)90074-8.

[110] M. A. C. Perryman, L. Lindegren, J. Kovalevsky, E. Hoeg, U. Bastian, P. L. Bernacca, M. Crézé, F. Donati, M. Grenon, M. Grewing, F. van Leeuwen, H. van der Marel,

F. Mignard, C. A. Murray, R. S. Le Poole, H. Schrijver, C. Turon, F. Arenou, M. Froeschlé, and C. S. Petersen. The HIPPARCOS Catalogue. A&A, 323:L49–L52, July 1997.

[111] P. Pinilla, M. Benisty, and T. Birnstiel. Ring shaped dust accumulation in transition disks. A&A, 545:A81, September 2012. doi: 10.1051/0004-6361/201219315.

[112] P. Pinilla, T. Birnstiel, L. Ricci, C. P. Dullemond, A. L. Uribe, L. Testi, and A. Natta. Trapping dust particles in the outer regions of protoplanetary disks. A&A, 538:A114, February 2012. doi: 10.1051/0004-6361/201118204.

[113] J. B. Pollack, O. Hubickyj, P. Bodenheimer, J. J. Lissauer, M. Podolak, and Y. Greenzweig. Formation of the Giant Planets by Concurrent Accretion of Solids and Gas. *Icarus*, 124:62–85, November 1996. doi: 10.1006/icar.1996.0190.

[114] K. M. Pontoppidan, G. A. Blake, and A. Smette. The Structure and Dynamics of Molecular Gas in Planet-forming Zones: A CRIRES Spectro-astrometric Survey. ApJ, 733:84, June 2011. doi: 10.1088/0004-637X/733/2/84.

[115] A. C. Quillen, P. Varnière, I. Minchev, and A. Frank. Driving Spiral Arms in the Circumstellar Disks of HD 100546 and HD 141569A. AJ, 129:2481–2495, May 2005. doi: 10.1086/428954.

[116] N. Raettig, H. Klahr, and W. Lyra. Particle Trapping and Streaming Instability in Vortices. *ArXiv e-prints*, January 2015.

[117] A. D. Railton and J. C. B. Papaloizou. On the local stability of vortices in differentially rotating discs. MNRAS, 445:4409–4426, December 2014. doi: 10.1093/mnras/stu2060.

[118] J. Rameau, G. Chauvin, A.-M. Lagrange, P. Thébault, J. Milli, J. H. Girard, and M. Bonnefoy. High-contrast imaging of the close environment of HD 142527. VLT/NaCo adaptive optics thermal and angular differential imaging. A&A, 546:A24, October 2012. doi: 10.1051/0004-6361/201219736.

[119] J. Rameau, G. Chauvin, A.-M. Lagrange, A. Boccaletti, S. P. Quanz, M. Bonnefoy, J. H. Girard, P. Delorme, S. Desidera, H. Klahr, C. Mordasini, C. Dumas, and M. Bonavita. Discovery of a Probable 4-5 Jupiter-mass Exoplanet to HD 95086 by Direct Imaging. ApJ, 772:L15, August 2013. doi: 10.1088/2041-8205/772/2/L15.

[120] Z. Regály, A. Juhász, Z. Sándor, and C. P. Dullemond. Possible planet-forming regions on submillimetre images. MNRAS, 419:1701–1712, January 2012. doi: 10.1111/j.1365-2966.2011.19834.x.

[121] T. J. Rodigas, K. B. Follette, A. Weinberger, L. Close, and D. C. Hines. Polarized Light Imaging of the HD 142527 Transition Disk with the Gemini Planet Imager: Dust around the Close-in Companion. ApJ, 791:L37, August 2014. doi: 10.1088/2041-8205/791/2/L37.

[122] K. A. Rosenfeld, C. Qi, S. M. Andrews, D. J. Wilner, S. A. Corder, C. P. Dullemond,

S.-Y. Lin, A. M. Hughes, P. D'Alessio, and P. T. P. Ho. Kinematics of the CO Gas in the Inner Regions of the TW Hya Disk. ApJ, 757:129, October 2012. doi: 10.1088/0004-637X/757/2/129.

[123] V. S. Safronov. *Evolution of the protoplanetary cloud and formation of the earth and planets.* 1972.

[124] V. S. Safronov and E. V. Zvjagina. Relative Sizes of the Largest Bodies during the Accumulation of Planets. *Icar*, 10:109–115, January 1969. doi: 10.1016/0019-1035(69)90013-X.

[125] A. Sicilia-Aguilar, L. Hartmann, N. Calvet, S. T. Megeath, J. Muzerolle, L. Allen, P. D'Alessio, B. Merín, J. Stauffer, E. Young, and C. Lada. Disk Evolution in Cep OB2: Results from the Spitzer Space Telescope. ApJ, 638:897–919, February 2006. doi: 10.1086/498085.

[126] D. Stamatellos, D. A. Hubber, and A. P. Whitworth. Brown dwarf formation by gravitational fragmentation of massive, extended protostellar discs. MNRAS, 382:L30–L34, November 2007. doi: 10.1111/j.1745-3933.2007.00383.x.

[127] K. M. Strom, S. E. Strom, S. Edwards, S. Cabrit, and M. F. Skrutskie. Circumstellar material associated with solar-type pre-main-sequence stars - A possible constraint on the timescale for planet building. AJ, 97:1451–1470, May 1989. doi: 10.1086/115085.

[128] H. Sung, J. R. Stauffer, and M. S. Bessell. A Spitzer View of the Young Open Cluster NGC 2264. AJ, 138:1116–1136, October 2009. doi: 10.1088/0004-6256/138/4/1116.

[129] P. Tanga, A. Babiano, B. Dubrulle, and A. Provenzale. Forming Planetesimals in Vortices. *Icarus*, 121:158–170, May 1996. doi: 10.1006/icar.1996.0076.

[130] J. Teiser and G. Wurm. High-velocity dust collisions: forming planetesimals in a fragmentation cascade with final accretion. MNRAS, 393:1584–1594, March 2009. doi: 10.1111/j.1365-2966.2008.14289.x.

[131] L. Testi, A. Natta, D. S. Shepherd, and D. J. Wilner. Large grains in the disk of CQ Tau. A&A, 403:323–328, May 2003. doi: 10.1051/0004-6361:20030362.

[132] A. Toomre. On the gravitational stability of a disk of stars. ApJ, 139:1217–1238, May 1964. doi: 10.1086/147861.

[133] R. van Boekel, M. Min, C. Leinert, L. B. F. M. Waters, A. Richichi, O. Chesneau, C. Dominik, W. Jaffe, A. Dutrey, U. Graser, T. Henning, J. de Jong, R. Köhler, A. de Koter, B. Lopez, F. Malbet, S. Morel, F. Paresce, G. Perrin, T. Preibisch, F. Przygodda, M. Schöller, and M. Wittkowski. The building blocks of planets within the 'terrestrial' region of protoplanetary disks. Nature, 432:479–482, November 2004. doi: 10.1038/nature03088.

[134] M. E. van den Ancker, D. de Winter, and H. R. E. Tjin A Djie. HIPPARCOS photometry of Herbig Ae/Be stars. A&A, 330:145–154, February 1998.

[135] N. van der Marel, E. F. van Dishoeck, S. Bruderer, T. Birnstiel, P. Pinilla, C. P. Dullemond, T. A. van Kempen, M. Schmalzl, J. M. Brown, G. J. Herczeg, G. S. Matthews, and V. Geers. A major asymmetric dust trap in a transition disk. *Science*, 340:1199–1202, 2013.

[136] F. van Leeuwen. Validation of the new Hipparcos reduction. A&A, 474:653–664, November 2007. doi: 10.1051/0004-6361:20078357.

[137] A. P. Verhoeff, M. Min, E. Pantin, L. B. F. M. Waters, A. G. G. M. Tielens, M. Honda, H. Fujiwara, J. Bouwman, R. van Boekel, S. M. Dougherty, A. de Koter, C. Dominik, and G. D. Mulders. The complex circumstellar environment of HD 142527. A&A, 528: A91, April 2011. doi: 10.1051/0004-6361/201014952.

[138] S. J. Weidenschilling. Aerodynamics of solid bodies in the solar nebula. MNRAS, 180: 57–70, July 1977.

[139] S. J. Weidenschilling. The distribution of mass in the planetary system and solar nebula. Ap&SS, 51:153–158, September 1977. doi: 10.1007/BF00642464.

[140] D. A. Weintraub, G. Sandell, and W. D. Duncan. Submillimeter measurements of T Tauri and FU Orionis stars. ApJ, 340:L69–L72, May 1989. doi: 10.1086/185441.

[141] F. L. Whipple. On certain aerodynamic processes for asteroids and comets. In A. Elvius, editor, *From Plasma to Planet*, page 211, 1972.

[142] J. P. Williams and L. A. Cieza. Protoplanetary Disks and Their Evolution. ARA&A, 49:67–117, September 2011. doi: 10.1146/annurev-astro-081710-102548.

[143] E. Winston, S. T. Megeath, S. J. Wolk, J. Muzerolle, R. Gutermuth, J. L. Hora, L. E. Allen, B. Spitzbart, P. Myers, and G. G. Fazio. A Combined Spitzer and Chandra Survey of Young Stellar Objects in the Serpens Cloud Core. ApJ, 669:493–518, November 2007. doi: 10.1086/521384.

[144] R. A. Wittenmyer, J. Horner, C. G. Tinney, R. P. Butler, H. R. A. Jones, M. Tuomi, G. S. Salter, B. D. Carter, F. E. Koch, S. J. O'Toole, J. Bailey, and D. Wright. The Anglo-Australian Planet Search. XXIII. Two New Jupiter Analogs. ApJ, 783:103, March 2014. doi: 10.1088/0004-637X/783/2/103.

[145] M. C. Wyatt. Evolution of Debris Disks. ARA&A, 46:339–383, September 2008. doi: 10.1146/annurev.astro.45.051806.110525.

[146] Z. Zhu and J. M. Stone. Dust Trapping by Vortices in Transitional Disks: Evidence for Non-ideal Magnetohydrodynamic Effects in Protoplanetary Disks. ApJ, 795:53, November 2014. doi: 10.1088/0004-637X/795/1/53.